

# Magnetization Switching of Single Magnetite Nanoparticles Monitored Optically

S. Adhikari<sup>1†</sup>, Y. Wang<sup>1,2†</sup>, P. Spaeth<sup>1</sup>, F. Scalerandi<sup>3</sup>, W. Albrecht<sup>3</sup>, J. Liu<sup>2</sup>, M. Orrit<sup>1\*</sup>

† These authors contributed equally to this work

<sup>1</sup> Huygens-Kamerlingh Onnes Laboratory, Leiden University; 2300 RA Leiden, The Netherlands

<sup>2</sup> School of Mechatronics Engineering, Harbin Institute of Technology; Harbin 150001, P. R. China

<sup>3</sup> Department of Sustainable Energy Materials, AMOLF; Science Park 104, 1098 XG Amsterdam, The Netherlands

\*Corresponding author. Email: [orrit@physics.leidenuniv.nl](mailto:orrit@physics.leidenuniv.nl)

**Magnetic nanomaterials record information as fast as picoseconds in computer memories but retain it for millions of years in ancient rocks. This exceedingly broad range of times is covered by hopping over a potential energy barrier through temperature<sup>1</sup>, ultrafast optical excitation for demagnetization<sup>2,3</sup> or magnetization manipulation<sup>4</sup>, mechanical stress<sup>5,6</sup>, or microwaves<sup>7</sup>. As switching depends on nanoparticle size, shape, orientation, and material properties, only single-nanoparticle studies can eliminate ensemble heterogeneity. Here, we push the sensitivity of photothermal magnetic circular dichroism<sup>8</sup> down to *individual* 20-nm magnetite nanoparticles. Single-particle magnetization curves display superparamagnetic to ferromagnetic behaviors, depending on size, shape, and orientation. Some nanoparticles undergo thermally activated switching on time scales of milliseconds to minutes. Surprisingly, the switching barrier appears to vary in time, leading to dynamical heterogeneity. Our observations will help to identify and eventually control the nanoscale parameters influencing the switching of magnetic nanoparticles, an important step for applications in many fields.**

Magnetic nanomaterials, including nanoparticles, promise numerous applications in fields as varied as nanotechnology for data storage, sensing, and logics<sup>9</sup>, geomagnetism<sup>10</sup>, magnetothermal therapy in medicine<sup>11</sup>, or the bio-magnetic compass of bacteria and birds<sup>12</sup>. In all those fields of application, however, the heterogeneity of magnetic nanomaterials is an obstacle to a better characterization and understanding of their magnetic properties. Single-nanoparticles studies<sup>13</sup> are required to overcome ensemble averaging, and open the correlation of magnetic properties with nanoparticle composition, size, shape<sup>14,15</sup>, orientation and structure<sup>16</sup>. Several techniques can reach single-nanoparticle magnetization sensitivity, from electrical current measurements<sup>17</sup> to scanning probe microscopies<sup>18–20</sup>. Those techniques, however, are complex and often require contacts and/or scanning probes. Non-contact optical techniques are thus particularly attractive. Setting aside X-ray MCD measurements at synchrotrons<sup>15</sup>,

conventional optical Kerr microscopy based on the magneto-optical Kerr effect (MOKE) lacks the spatial resolution needed to address single nanoparticles, with the notable exception of magnetometry with NV-centers in diamond.<sup>21</sup> We recently proposed an original optical technique, photothermal magnetic circular dichroism (PT MCD) microscopy<sup>8</sup>, which has the potential to optically record (time-resolved) magnetic properties of single magnetic nanoparticles. In this work, we demonstrate the experimental imaging of single 20-nm magnetite nanoparticles and we record their full magnetization curves, one particle at a time. In this method, the single-particle MOKE signal, which gives rise to a slight difference in optical absorption for right- and left-circularly polarized light, is detected by scattering of a probe beam. The resulting magnetization curves hold information about the superparamagnetic or ferromagnetic state of the particles, about their magnetic anisotropy and orientation. In addition, our technique is able to unravel thermally activated switching between two antiparallel magnetization states, and to visualize these switching events with a time resolution down to ten milliseconds. This phenomenon, predicted by Néel some 70 years ago, can now be followed by our technique in real time on single magnetite particles, the type of particles which are thought to have recorded paleomagnetic data in ancient rocks. By varying the applied magnetic field and temperature, we deduce the particles' magnetic dipoles, a few  $10^5$  Bohr magnetons, and the switching barrier's activation energies, around 0.7 eV. Long switching time traces display pronounced changes in switching rate, i.e., dynamical heterogeneity, indicating that the barrier energy fluctuates significantly with time.

Figure 1(A) shows a photothermal (PT) image of six single magnetite nanoparticles, labeled P1 to P6, with diameters ranging from about 19 nm to 25 nm. The sizes, mentioned in the inset in Fig. 1(E-J), are deduced from a comparison of the average photothermal signal of a large number of such nanoparticles (see Fig. S1) to their average diameter, about 19 nm, obtained from transmission electron microscope (TEM) images of 38 particles (see Fig. S2) and assuming a linear relationship between a particle's photothermal signal and its volume. A histogram of signal-to-background ratios of 465 single magnetite nanoparticles is shown in Fig. S1, with a mean signal-to-background (S/B) ratio of about 40. Such a high visibility indicates that even smaller magnetite nanoparticles could be detected with our photothermal setup.

By modulating the heating beam between right- and left-handed circular polarizations, we observe the circular dichroism (CD) response of particles P1 to P6, first in the absence of a magnetic field (Fig. 1B). We assign most of the weak signals observed to geometric CD stemming from a low but non-zero dielectric polarizability of magnetite at our pump wavelength of 532 nm, and from non-mirror-symmetrical (chiral) particle shapes. The significant and consistent positive signal of particle P5, however, suggests a possible ferromagnetic behavior. Upon application of a static magnetic field of  $\pm (283 \pm 6)$  mT along the microscope's optical axis, all particles acquire strong CD signals, which change sign with the field direction (Fig. 1C, D), indicating magnetic circular dichroism (MCD). The signal/noise (S/N) ratio exceeds 10 for an integration time of 100 ms/pixel, demonstrating the high sensitivity of the technique (note that we use S/N instead of S/B for the MCD signal because the MCD background fluctuates around zero). The saturation magnetic moment expected for particle P1 can be deduced from its volume

and from the side of the cubic unit cell of magnetite, 0.839 nm. With 32 Bohr magnetons per unit cell<sup>22</sup>, we expect a magnetic moment of  $4.4 \times 10^5$  Bohr magnetons at saturation.

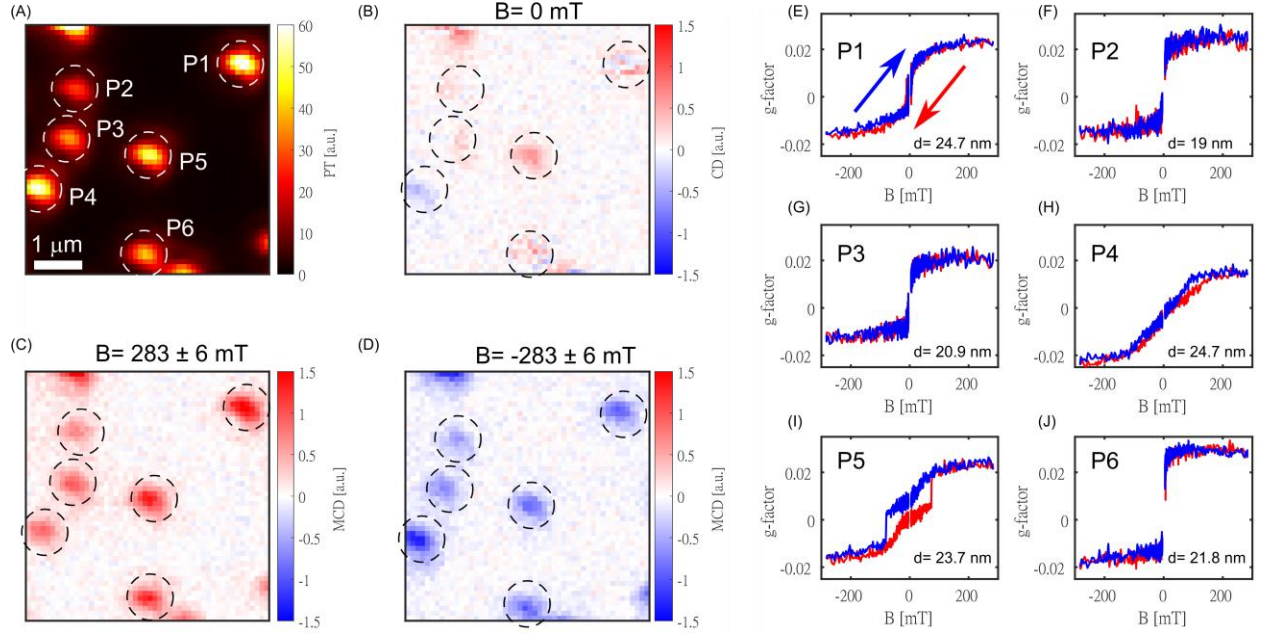


*Fig. 1: Photothermal CD images of single magnetite nanoparticles, about 20 nm in diameter. A: Photothermal (PT) image; B: CD image without applied static magnetic field; C, D: MCD images with magnetic field applied along the microscope's optical axis ( $\pm 283$  mT, respectively); the signal units of images (A-D) are mutually consistent; E-J: Dependence of the g-factor on magnetic field for the six nanoparticles P1 to P6. The average diameters of the particles deduced from their PT signal are mentioned in the inset. Particle P1 shows switching between positive and negative g-factors at weak fields, whereas particle P5 shows hysteresis. The colors indicate the scan direction of the applied field as indicated in (E).*

Our MCD measurements enable us to record the full magnetization curves of single magnetite particles. From the magneto-optical signal  $MCD = (I_- - I_+)$ , i.e., the difference in circularly left- ( $I_-$ ) and right- ( $I_+$ ) polarized absorption, and from the unpolarized photothermal absorption,  $PT = (I_- + I_+)/2$ , we deduce the dissymmetry or g-factor,  $g = 2 \frac{I_- - I_+}{I_- + I_+}$ . The magnetization curves of particles P1 to P6 in Fig. 1E-J show that the magnetic properties of individual particles are strikingly distinct. According to the Néel-Brown model<sup>23</sup>, superparamagnetism is observed when the switching is much faster than the measurement time, whereas ferromagnetism is observed in the opposite limit. Particles P2, P3, P4 and P6 display superparamagnetic behavior, with a regular increase of magnetization with applied field. In contrast, particle P5 shows a typical ferromagnetic behavior indicated by a clear hysteresis loop and a coercive field of about 100 mT. Superparamagnetic particles P2, P3 and P6 show saturation at much lower fields than particle P4. We attribute this difference to the orientation of

the magnetic easy axis, which is presumably nearly aligned with the field for particles P2, P3, and P6, but nearly perpendicular to it for particle P4. The magnetization curves can be qualitatively understood and fitted within the Stoner-Wohlfarth model<sup>24</sup> (discussed in more detail in the Supplementary Material, see Fig. S3-S6), which assumes that size and shape anisotropy determine the energy barrier between two opposite magnetization states. From this analysis, we fitted the magnetization curves of P2, P3, P4, and P6 (see Fig. S7) with aspect ratios (1.2, 1.4, 1.8, 1.2) and easy axis angles ( $50^\circ$ ,  $50^\circ$ ,  $90^\circ$ ,  $40^\circ$ ) with the applied magnetic field, respectively. The magnetization curves of 32 more single particles are presented in Figs. S8, S9 of the Supplementary Material. The low slope of particle P4 is assigned to a high aspect ratio of the particle and to the orientation of its long, easy axis nearly in the sample plane. Particle P1 shows intermediate behavior, suggesting that magnetic switching might occur during the measurement.

As is apparent from the large fluctuations in the MCD signal of particle P1 (see Fig. 1B), it behaves very differently from the other particles. This is confirmed by the large spread of positive and negative g-factors for small field values (Fig. 1E). These fluctuations suggest single-particle magnetic switching. We recorded a 100-s MCD time trace of P1 (Fig. 2A) without an applied field, and indeed find several switching events separated by several seconds on average. We also measured linear dichroism (LD) signals, which do not show any switching (see Fig. S10). As the magnetite particles are mostly single-crystalline (Fig. S2), we assume that our particles have a single magnetic domain, where exchange energy is minimized by alignment of all spins, producing a macro-spin. We assign the observed switching events to flips of the macro-spin of particle P1 between two (magnetic-field-dependent) antiparallel states, which we label ‘up’ and ‘down’. From the Néel-Brown theory, we expect switching to be influenced by an applied magnetic field, as we indeed find in our study of the populations of up- and down-levels.

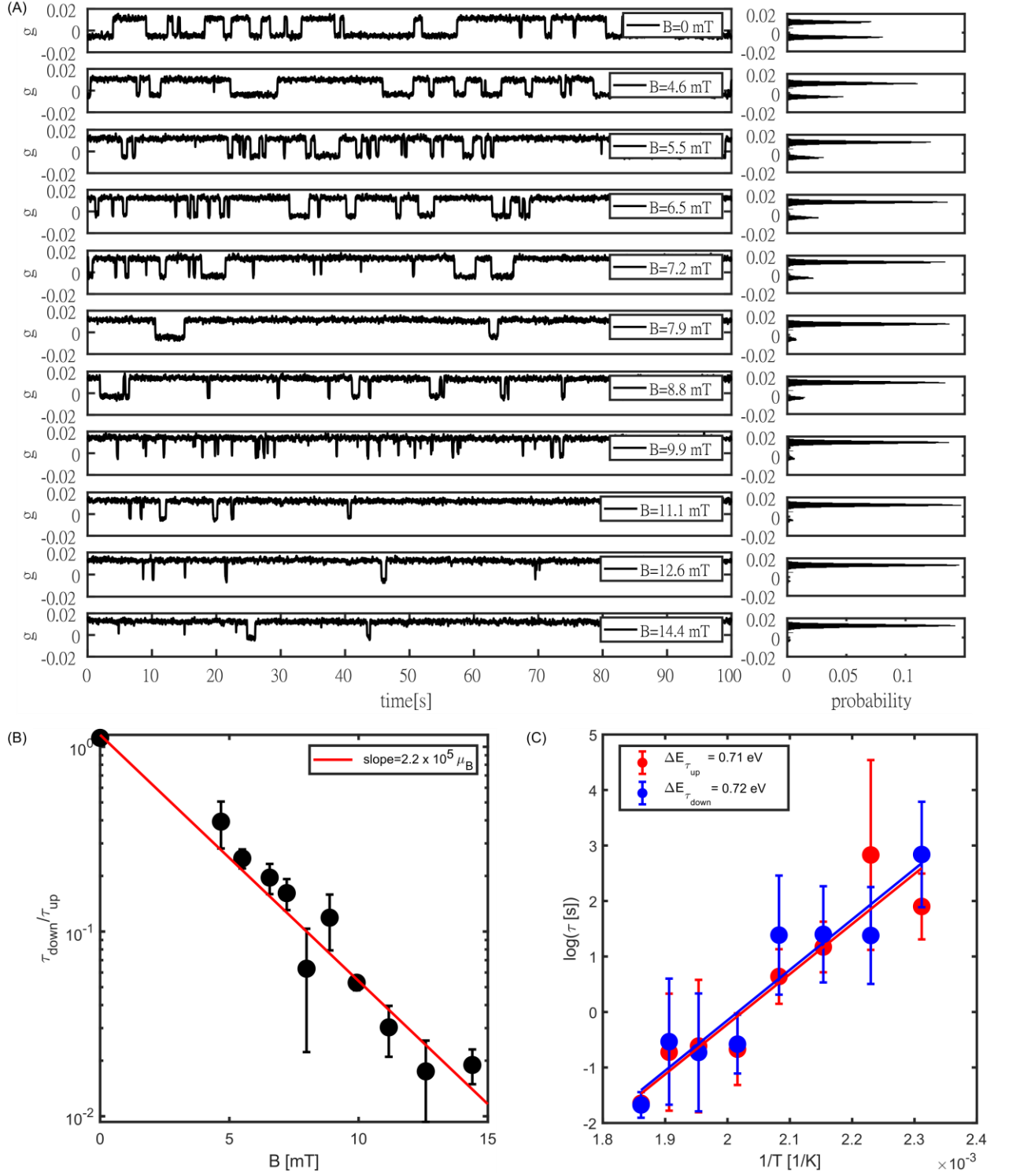


Fig. 2: Magnetization switching of a single magnetite nanoparticle (particle P1 of Fig. 1) and dependence of the occupation of the two states on magnetic field ( $B$ ) and on temperature ( $T$ ). **A:** Magnetization time traces showing switching at different magnetic fields. **B:** Ratio of down- and up-times,  $\tau_{\text{down}}/\tau_{\text{up}}$  versus  $B$  with a fit according to the Stoner-Wohlfarth model. The fit slope (inset),  $2\mu\cos\psi/k_B T$ , provides the particle's magnetic moment. **C:** Temperature dependence of

*up- and down-times ( $\tau_{up}$  and  $\tau_{down}$ ) fitted with an Arrhenius law, which provides an energy barrier of  $0.7 \pm 0.2$  eV mentioned in the inset. The error bars are the standard deviations of three measurements at a given temperature.*

Switching time traces of P1 were recorded over 100 s for applied fields varying from 0 to 15 mT, and are presented in Fig. 2A. The population of the up-state (positive g-factor) increases with the magnetic field. Above 15 mT, mostly the up-state is occupied, as can also be seen in Fig. 1E. A further, weak increase in g-factor, i.e., in magnetization, takes place at higher fields. We assign it to the gradual orientation of the saturated macro-spin along the external magnetic field. Further details of the Stoner-Wohlfarth fit are given in the Supplementary Material (Fig. S3). Figure 2A presents histograms of g-factors for each time trace, which allow us to perform a threshold analysis and to determine the up- ( $\tau_{up}$ ) and down- ( $\tau_{down}$ ) residence times (see Fig. S11). By fitting the ratio of these times with the Stoner-Wohlfarth model (Fig. 2B), we obtain a slope of  $2.05 \times 10^5$  Bohr magnetons. This slope is approximately given by  $2\mu \cos \psi / k_B T$ , where  $\mu$  is the magnetic moment,  $\psi$  is the angle between the easy axis and the applied magnetic field,  $k_B$  is Boltzmann's constant and  $T$  is the absolute temperature. The angle  $\psi$  can be determined from a fit to the magnetization curve, as shown in Fig. S5, and was found to be about  $70^\circ \pm 10^\circ$  in the present case. Therefore, we deduce a magnetic moment of the particle of about  $3 \times 10^5$  Bohr magnetons, which is reasonably close to the above estimate ( $4.4 \times 10^5$  Bohr magnetons). The slight difference between these two values might arise from a magnetic dead layer close to the nanoparticle's surface, i.e., a layer of ill-aligned or disordered spins<sup>25</sup>. A magnetic dead layer with a shell thickness of 1.5 nm would explain the difference between experimental and expected estimates. The switching behavior of two more particles as a function of applied magnetic field is presented in Figs. S12, S13.



The Néel-Brown theory<sup>23</sup> of superparamagnetism assigns macro-spin switching to activated barrier crossing, with a rate following an Arrhenius dependence on temperature. To vary the temperature in our measurements, we have varied the laser power of the probe beam, which is tightly focused on the particle under study. Based on literature values of the absorption of magnetite and on COMSOL simulations we estimated the temperature to vary from 432 K to 537 K in the range of probe powers we used (see Supplementary Material, Figs. S14, S15). We present the population ratio of up-state and down-state as an Arrhenius plot (Fig. 2C). However, as will be discussed below, the switching rate was found to fluctuate significantly, even at a fixed temperature. We therefore had to average several measurements for each temperature, causing the fairly large error bars in Fig. 2C. The slope of the plot provides an energy barrier of about 0.7 eV for particle P1, which is considerably higher than the thermal energy  $k_B T$  (0.04 – 0.05 eV). Such a large barrier combined with the exponential Arrhenius dependence explains why switching rates cover many orders of magnitude of times within a comparatively narrow range of temperatures.

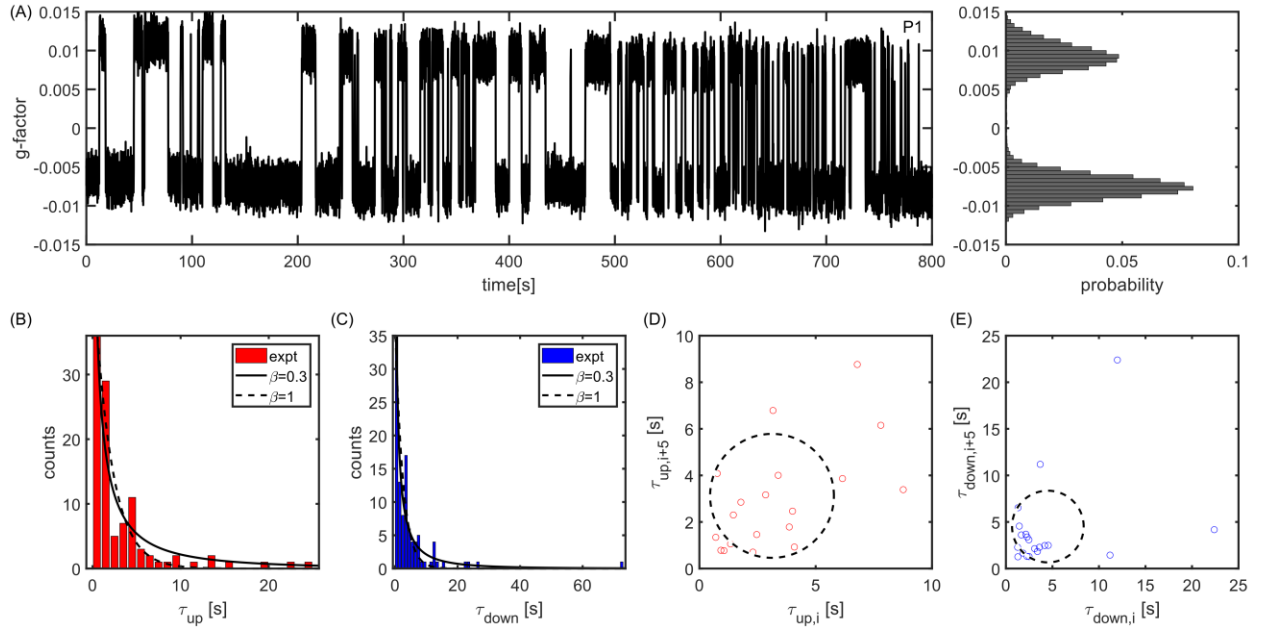


**Fig. 3: Dynamical heterogeneity of magnetization switching of particle P1. A:** Time trace of magnetization switching over 800 s. The corresponding histogram of g-factors is shown on the right. **B, C:** Histograms of  $\tau_{up}$  and  $\tau_{down}$  with stretched-exponential fits (stretching exponents  $\beta$  given in insets). **D, E:** Correlation plots of successive averages of  $\tau_{up}$  and  $\tau_{down}$ , averaged over five successive events. Strong fluctuations of these averages lead to correlation points out of the dashed discs (see details in the main text).

Finally, we come back to the aforementioned fluctuations of the barrier rate. Figure 3A shows a magnetization switching trace of particle P1 over a longer duration of 800 s. The switching behavior is obviously much faster in the time interval between 600 s and 700 s than at the beginning of the trace, although experimental conditions did not change. Similar rate changes of an activated process are well known in single-molecule traces of complex systems such as

enzymes under the concept of dynamical heterogeneity.<sup>26</sup> Histograms of residence times  $\tau_{\text{up}}$  and  $\tau_{\text{down}}$  in the two states are shown in Fig. 3B, C. These histograms present excess events at long times compared to single exponentials. We fitted them with stretched exponentials, with stretching exponents of 0.61 and 0.55 for  $\tau_{\text{up}}$  and  $\tau_{\text{down}}$ , respectively. To further prove dynamical heterogeneity, we have used a statistical tool<sup>27</sup> developed earlier for single protein molecules. After coarse-graining the trace by averaging five consecutive up-times and down-times to reduce statistical fluctuations, we correlate consecutive averaged times for up and down states, separately. The corresponding scatter plots are shown in Fig. 3D, E. A simulation with an exponential distribution of times gives correlated points concentrated (with 95 % probability) in the dotted circles indicated in Fig. 3D, E. The many experimental points falling well outside these areas confirm that the switching rate itself fluctuates strongly. Similar results are found for another particle monitored over several hours (see Fig. S16). This particle started as superparamagnetic, then switched to a ferromagnetic behavior, as we verified by measuring a hysteresis loop. After 30 minutes without exposure to laser light, the particle returned to its initial superparamagnetic behavior, and gradually drifted towards ferromagnetism again. After two days in the dark, the particle had returned to a superparamagnetic state.

Dynamical heterogeneity is most often seen as arising from variations of the reaction barrier, through slow conformational changes for proteins<sup>26,27</sup>, or through changes of the magnetic energy landscape in the case of magnetic nanoparticles<sup>10,15,28</sup>. Transitions from ferromagnetism to superparamagnetism have been reported previously<sup>28</sup> for single iron nanoparticles. In the specific case of magnetite, we speculate that the oxidation state of some iron ions may change through electron transfer or upon oxidation in air, particularly at the elevated temperatures (up to 500 K) caused by laser heating. The resulting changes in the spatial distribution of  $\text{Fe}^{2+}$  and  $\text{Fe}^{3+}$  ions, or in the surface binding of ligands by photo- (or temperature-) driven chemistry could change the magnetic energy landscape.<sup>10,16</sup> Additional experiments, such as removal of organic ligands by plasma etching, or ALD coating the particles with 5 nm of  $\text{HfO}_2$  (see Figs. S17, S18, S19) could not provide any clear indication of a surface origin of dynamical heterogeneity. Further experiments are needed to explore the role of experimental parameters in switching barrier fluctuations.

In this work, we have imaged and studied individual magnetite nanoparticles of 20 nm in diameter by pure optical means. Although they had similar sizes, these particles turned out to be ferromagnetic, super-paramagnetic, or to switch between two antiparallel magnetization states on time scales of milliseconds to minutes. Such information has so far been hidden in ensemble-averaged experiments. The various magnetization curves of single nanoparticles were explained in a simple Stoner-Wohlfarth model, with the anisotropy aspect ratio and the angle of the easy magnetization axis as only fit parameters, adjusted for each particle. The magnetic-field dependence of thermally assisted switching provided us with an estimated magnetic moment of a single magnetite nanoparticle of  $10^5$  Bohr magnetons. An anisotropy energy barrier of about 0.7 eV was obtained from the temperature dependence of the switching. The switching rate was found to fluctuate over time, revealing dynamical heterogeneity found earlier in other complex nanometer-scale systems. Our experiments demonstrate the versatility of our technique and the richness of information that can be gained at the single-particle level by optical means alone, and



open new possibilities to explore the influence of composition, surfaces and defects on nano-magnetic switching.

## References

- (1) Li, X.; Zanolini, T.; Wang, T.; Zhu, K.; Puglisi, F. M.; Lanza, M. Random Telegraph Noise in Metal-Oxide Memristors for True Random Number Generators: A Materials Study. *Advanced Functional Materials* **2021**, *31* (27), 2102172. <https://doi.org/10.1002/adfm.202102172>.
- (2) Tauchert, S. R.; Volkov, M.; Ehberger, D.; Kazenwadel, D.; Evers, M.; Lange, H.; Donges, A.; Book, A.; Kreuzpaintner, W.; Nowak, U.; Baum, P. Polarized Phonons Carry Angular Momentum in Ultrafast Demagnetization. *Nature* **2022**, *602* (7895), 73–77. <https://doi.org/10.1038/s41586-021-04306-4>.
- (3) Koopmans, B.; Malinowski, G.; Dalla Longa, F.; Steiauf, D.; Fähnle, M.; Roth, T.; Cinchetti, M.; Aeschlimann, M. Explaining the Paradoxical Diversity of Ultrafast Laser-Induced Demagnetization. *Nature Mater* **2010**, *9* (3), 259–265. <https://doi.org/10.1038/nmat2593>.
- (4) Kirilyuk, A.; Kimel, A. V.; Rasing, T. Ultrafast Optical Manipulation of Magnetic Order. *Rev. Mod. Phys.* **2010**, *82* (3), 2731–2784. <https://doi.org/10.1103/RevModPhys.82.2731>.
- (5) Song, T.; Fei, Z.; Yankowitz, M.; Lin, Z.; Jiang, Q.; Hwangbo, K.; Zhang, Q.; Sun, B.; Taniguchi, T.; Watanabe, K.; McGuire, M. A.; Graf, D.; Cao, T.; Chu, J.-H.; Cobden, D. H.; Dean, C. R.; Xiao, D.; Xu, X. Switching 2D Magnetic States via Pressure Tuning of Layer Stacking. *Nat. Mater.* **2019**, *18* (12), 1298–1302. <https://doi.org/10.1038/s41563-019-0505-2>.
- (6) Li, T.; Jiang, S.; Sivadas, N.; Wang, Z.; Xu, Y.; Weber, D.; Goldberger, J. E.; Watanabe, K.; Taniguchi, T.; Fennie, C. J.; Fai Mak, K.; Shan, J. Pressure-Controlled Interlayer Magnetism in Atomically Thin CrI<sub>3</sub>. *Nat. Mater.* **2019**, *18* (12), 1303–1308. <https://doi.org/10.1038/s41563-019-0506-1>.
- (7) Okamoto, S.; Kikuchi, N.; Kitakami, O. Magnetization Switching Behavior with Microwave Assistance. *Appl. Phys. Lett.* **2008**, *93* (10), 102506. <https://doi.org/10.1063/1.2977474>.
- (8) Spaeth, P.; Adhikari, S.; Lahabi, K.; Baaske, M. D.; Wang, Y.; Orrit, M. Imaging the Magnetization of Single Magnetite Nanoparticle Clusters via Photothermal Circular Dichroism. *Nano Lett.* **2022**. <https://doi.org/10.1021/acs.nanolett.2c00178>.
- (9) Costache, M. V.; Sladkov, M.; Watts, S. M.; van der Wal, C. H.; van Wees, B. J. Electrical Detection of Spin Pumping Due to the Precessing Magnetization of a Single Ferromagnet. *Phys. Rev. Lett.* **2006**, *97* (21), 216603. <https://doi.org/10.1103/PhysRevLett.97.216603>.
- (10) Winklhofer, M.; Fabian, K.; Heider, F. Magnetic Blocking Temperatures of Magnetite Calculated with a Three-Dimensional Micromagnetic Model. *Journal of Geophysical Research: Solid Earth* **1997**, *102* (B10), 22695–22709. <https://doi.org/10.1029/97JB01730>.
- (11) Colombo, M.; Carregal-Romero, S.; Casula, M. F.; Gutiérrez, L.; Morales, M. P.; Böhm, I. B.; Heverhagen, J. T.; Prosperi, D.; Parak, W. J. Biological Applications of Magnetic Nanoparticles. *Chem. Soc. Rev.* **2012**, *41* (11), 4306–4334. <https://doi.org/10.1039/C2CS15337H>.
- (12) Wiltschko, R.; Schiffner, I.; Fuhrmann, P.; Wiltschko, W. The Role of the Magnetite-Based Receptors in the Beak in Pigeon Homing. *Current Biology* **2010**, *20* (17), 1534–1538. <https://doi.org/10.1016/j.cub.2010.06.073>.
- (13) Wernsdorfer, W.; Orozco, E. B.; Hasselbach, K.; Benoit, A.; Barbara, B.; Demoncy, N.; Loiseau, A.; Pascard, H.; Mailly, D. Experimental Evidence of the Néel-Brown Model of Magnetization Reversal. *Phys. Rev. Lett.* **1997**, *78* (9), 1791–1794. <https://doi.org/10.1103/PhysRevLett.78.1791>.

- (14) Moreno, R.; Poyser, S.; Meilak, D.; Meo, A.; Jenkins, S.; Lazarov, V. K.; Vallejo-Fernandez, G.; Majetich, S.; Evans, R. F. L. The Role of Faceting and Elongation on the Magnetic Anisotropy of Magnetite Fe<sub>3</sub>O<sub>4</sub> Nanocrystals. *Sci Rep* **2020**, *10* (1), 2722. <https://doi.org/10.1038/s41598-020-58976-7>.
- (15) Kleibert, A.; Balan, A.; Yanes, R.; Derlet, P. M.; Vaz, C. A. F.; Timm, M.; Fraile Rodríguez, A.; Béché, A.; Verbeeck, J.; Dhaka, R. S.; Radovic, M.; Nowak, U.; Nolting, F. Direct Observation of Enhanced Magnetism in Individual Size- and Shape-Selected 3d Transition Metal Nanoparticles. *Phys. Rev. B* **2017**, *95* (19), 195404. <https://doi.org/10.1103/PhysRevB.95.195404>.
- (16) Elnaggar, H.; Graas, S.; Lafuerza, S.; Detlefs, B.; Tabiś, W.; Gala, M. A.; Ismail, A.; van der Eerden, A.; Sikora, M.; Honig, J. M.; Glatzel, P.; de Groot, F. Temperature-Driven Self-Doping in Magnetite. *Phys. Rev. Lett.* **2021**, *127* (18), 186402. <https://doi.org/10.1103/PhysRevLett.127.186402>.
- (17) Hayakawa, K.; Kanai, S.; Funatsu, T.; Igarashi, J.; Jinnai, B.; Borders, W. A.; Ohno, H.; Fukami, S. Nanosecond Random Telegraph Noise in In-Plane Magnetic Tunnel Junctions. *Phys. Rev. Lett.* **2021**, *126* (11), 117202. <https://doi.org/10.1103/PhysRevLett.126.117202>.
- (18) Natterer, F. D.; Yang, K.; Paul, W.; Willke, P.; Choi, T.; Greber, T.; Heinrich, A. J.; Lutz, C. P. Reading and Writing Single-Atom Magnets. *Nature* **2017**, *543* (7644), 226–228. <https://doi.org/10.1038/nature21371>.
- (19) Hevroni, A.; Tsukerman, B.; Markovich, G. Probing Magnetization Dynamics in Individual Magnetite Nanocrystals Using Magnetoresistive Scanning Tunneling Microscopy. *Phys. Rev. B* **2015**, *92* (22), 224423. <https://doi.org/10.1103/PhysRevB.92.224423>.
- (20) Piotrowski, S. K.; Matty, M. F.; Majetich, S. A. Magnetic Fluctuations in Individual Superparamagnetic Particles. *IEEE Transactions on Magnetics* **2014**, *50* (11), 1–4. <https://doi.org/10.1109/TMAG.2014.2321327>.
- (21) Schmid-Lorch, D.; Häberle, T.; Reinhard, F.; Zappe, A.; Slota, M.; Bogani, L.; Finkler, A.; Wrachtrup, J. Relaxometry and Dephasing Imaging of Superparamagnetic Magnetite Nanoparticles Using a Single Qubit. *Nano Lett.* **2015**, *15* (8), 4942–4947. <https://doi.org/10.1021/acs.nanolett.5b00679>.
- (22) Askeland, D. R.; Fulay, P. P.; Wright, W. J. *The Science and Engineering of Materials.*, 6th ed.; 2010.
- (23) Brown, W. F. Thermal Fluctuations of a Single-Domain Particle. *Phys. Rev.* **1963**, *130* (5), 1677–1686. <https://doi.org/10.1103/PhysRev.130.1677>.
- (24) Stoner, E. C.; Wohlfarth, E. P. A Mechanism of Magnetic Hysteresis in Heterogeneous Alloys. *Philosophical Transactions of the Royal Society of London. Series A, Mathematical and Physical Sciences* **1948**, *240* (826), 599–642. <https://doi.org/10.1098/rsta.1948.0007>.
- (25) Dutta, P.; Pal, S.; Seehra, M. S.; Shah, N.; Huffman, G. P. Size Dependence of Magnetic Parameters and Surface Disorder in Magnetite Nanoparticles. *Journal of Applied Physics* **2009**, *105* (7), 07B501. <https://doi.org/10.1063/1.3055272>.
- (26) Lu, H. P.; Xun, L.; Xie, X. S. Single-Molecule Enzymatic Dynamics. *Science* **1998**, *282* (5395), 1877–1882. <https://doi.org/10.1126/science.282.5395.1877>.
- (27) Pradhan, B.; Engelhard, C.; Mulken, S. V.; Miao, X.; Canters, G. W.; Orrit, M. Single Electron Transfer Events and Dynamical Heterogeneity in the Small Protein Azurin from *Pseudomonas Aeruginosa*. *Chem. Sci.* **2020**, *11* (3), 763–771. <https://doi.org/10.1039/C9SC05405G>.
- (28) Balan, A.; Derlet, P. M.; Rodríguez, A. F.; Bansmann, J.; Yanes, R.; Nowak, U.; Kleibert, A.; Nolting, F. Direct Observation of Magnetic Metastability in Individual Iron Nanoparticles. *Phys. Rev. Lett.* **2014**, *112* (10), 107201. <https://doi.org/10.1103/PhysRevLett.112.107201>.

(29) Spaeth, P.; Adhikari, S.; Baaske, M. D.; Pud, S.; Ton, J.; Orrit, M. Photothermal Circular Dichroism of Single Nanoparticles Rejecting Linear Dichroism by Dual Modulation. *ACS Nano* **2021**, *15* (10), 16277–16285. <https://doi.org/10.1021/acsnano.1c05374>.

**Acknowledgments:** We acknowledge Jacqueline A. Labra-Muñoz for her contribution concerning the ALD deposition, performed at the Kavli Institute of Nanoscience in Delft University of Technology, financed by NWO through Nanofront project number NF17SYN.

**Funding:** OTP 16008 for PS, Spinoza Orrit for SA, CSC for YW

**Author contributions:** SA and MO planned the research, PS realized and adjusted the PT microscope, SA and YW did the measurements, YW did the SW model simulations, FS and WA did TEM measurements; all authors contributed in writing and discussing the manuscript.

**Competing interests:** Authors declare that they have no competing interests.

**Data and materials availability:** All data are available in the main text or the supplementary materials.

### **Supplementary Material:**

Supplementary material is available for this paper.

## **Methods**

### Sample preparation

Magnetite ( $\text{Fe}_3\text{O}_4$ ) nanoparticles 20 nm in diameter, coated with polyvinylpyrrolidone (PVP) were purchased from Nanocomposix (product number: MGPB20). Hexadecane was purchased from Sigma-Aldrich (product number: H6703). The stock solution of the magnetite nanoparticles was diluted 1,000 times in an aqueous solution. The diluted solution was spin-coated on a UV-plasma-cleaned glass coverslip (thickness about 170  $\mu\text{m}$ ) to disperse the particles homogeneously on the glass surface. The glass coverslip was sandwiched with a cavity glass slide with a thickness of about 1.4 mm which contained a cavity to hold the liquid used for the photothermal measurement (i.e., hexadecane). All the measurements mentioned in the main text were done on magnetite nanoparticles immersed in hexadecane. In some measurements reported in the supplementary section, magnetite nanoparticles were measured in immersion oil. In that case, the same immersion oil used for the microscope objective was used as the photothermal medium.

### Optical setup:

The details of the optical setup are described in our recent publication.<sup>8</sup> Here we give a brief description of the setup. The heating laser of wavelength of 532 nm was passed through an electro-optical modulator (EOM) and a photo-elastic modulator (PEM) which modulated the laser's polarization at frequencies of 33.5 kHz and 50 kHz, respectively. The dual modulation of the laser polarization created a circular dichroism (CD) signal at the sum frequency as discussed in our previous publication<sup>29</sup>. The heating laser was focused in the back-focal plane of the immersion-oil objective (NA= 1.45) and illuminated the sample in a wide-field area of about

3  $\mu\text{m}$  diameter. The collimated circularly polarized continuous-wave probe beam of wavelength of 780 nm was focused at the sample using the same objective. The scattered probe beam was detected in the reflection mode, and was filtered from the heating beam using a band-pass filter (BP780) and focused on a photodiode using a lens of focal length of 75 mm. The CD signal at the sum frequency i.e., 83.5 kHz was detected using a lock-in amplifier. To vary the magnetic field, a long permanent cylindrical NdFeB magnet (a set of small cylindrical magnets of diameter of 3 mm) was placed perpendicular to the sample and its position was varied to change the field. To invert the direction of the magnetic field, the magnetic poles were inverted.

# Supplementary Material for

## **Magnetization Switching of Single Magnetite Nanoparticles Monitored Optically**

S. Adhikari<sup>1†</sup>, Y. Wang<sup>1,2†</sup>, P. Spaeth<sup>1</sup>, F. Scalerandi<sup>3</sup>, W. Albrecht<sup>3</sup>, J. Liu<sup>2</sup>, M. Orrit<sup>1\*</sup>

† These authors contributed equally to this work

<sup>1</sup> Huygens-Kamerlingh Onnes Laboratory, Leiden University; 2300 RA Leiden, The Netherlands

<sup>2</sup> School of Mechatronics Engineering, Harbin Institute of Technology; Harbin 150001, P. R. China

<sup>3</sup> Department of Sustainable Energy Materials, AMOLF; Science Park 104, 1098 XG Amsterdam, The Netherlands

\*Corresponding author. Email: [orrit@physics.leidenuniv.nl](mailto:orrit@physics.leidenuniv.nl)

### Photothermal imaging of single magnetite nanoparticles in hexadecane

To estimate the size of a single magnetite nanoparticle from photothermal measurements, we performed photothermal imaging of many single magnetite nanoparticles as shown in Figure S4. A total of 465 single magnetite nanoparticles were detected and a histogram of their photothermal signals is shown in the same figure. Aggregates are distinguished by their very strong photothermal signals and were not considered in the histogram. The peak value of the photothermal histogram corresponds to particles with size of about 19 nm which is obtained from TEM measurements as shown in Figure S5. A histogram of signal-to-background ratios of 465 single magnetite nanoparticles is also shown in Figure S4. The peak value is about 40 for about 19 nm diameter particles. Such a high signal-to-background ratio indicates that magnetite nanoparticles smaller than 19 nm can be detected in photothermal imaging.



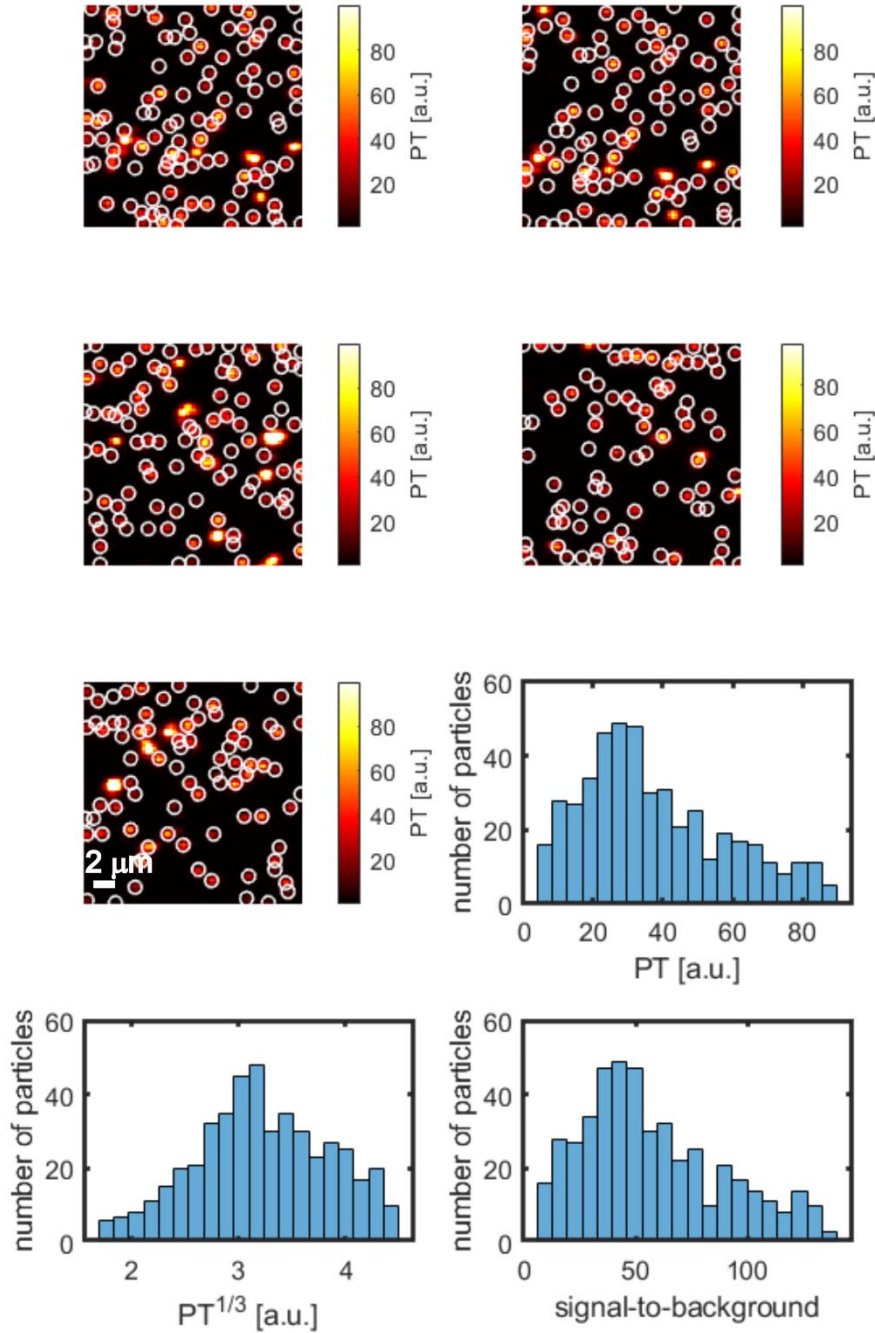


*Figure S4: Photothermal measurements of single magnetite particles in five different regions. Single particles and aggregates are distinguished by their PT strength. Only single particles are marked with white circles. The distribution of the maximum photothermal signals of 465 single particles is shown. The peak value of about 27 a. u. corresponds to about 19 nm magnetite particle as shown in Fig. S2. The size mentioned in Figure 1 in the main text is calculated based on this calibration measurement. The cubic root of the PT signal corresponds to the size of a particle. A histogram of signal-to-background ratios for the 465 single particles is also shown.*

### TEM images of single magnetite nanoparticles

To get an idea of the size and shape of single magnetite nanoparticles and their crystallinity, we performed transmission electron microscopy (TEM) imaging as shown in Figure S5. From the TEM images, it is evident that most particles are single-crystalline and heterogeneous in their sizes and shapes. Most particles have asymmetric shapes. To calculate the size of each particle, the volume of each particle assimilated to a prolate ellipsoid is calculated. From the ellipsoid volume, the effective average diameter of the particle is calculated considering it as a spherical volume. The average diameter obtained from 38 single particles is  $19 \text{ nm} \pm 0.5 \text{ nm}$ , i.e., close to the size of about 20 nm provided by the manufacturer.

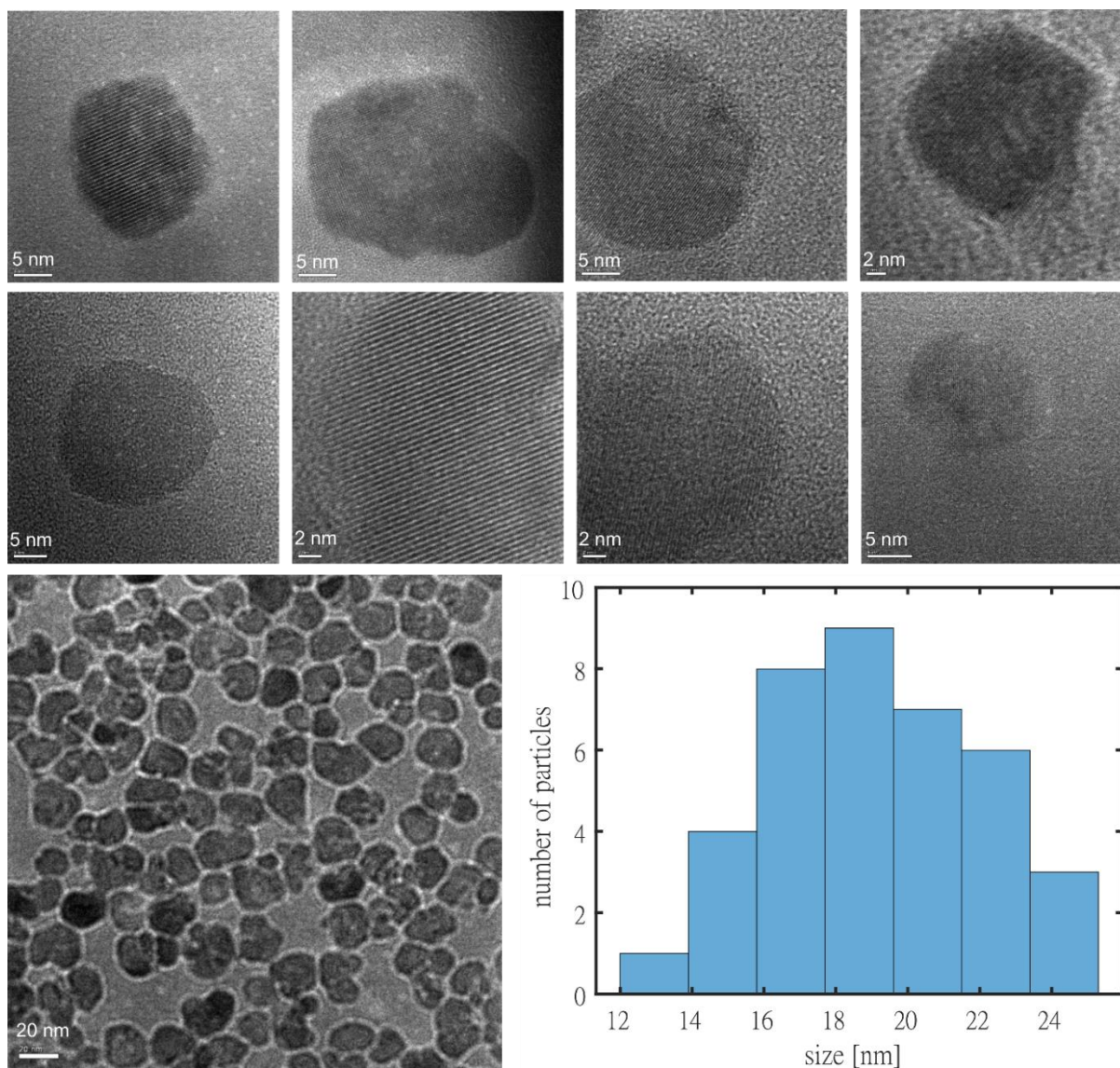


*Figure S5: The top two rows show TEM images of eight single-crystalline magnetite nanoparticles. (Bottom left) TEM image of many single magnetite nanoparticles showing heterogeneity in size and shape. The image was taken slightly out-of-focus for easier*

identification of particle boundaries. (Bottom right) Histogram of effective diameters of single particles determined from the TEM data.

### Stoner-Wohlfarth model

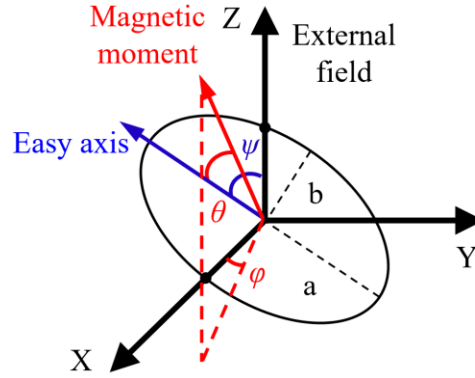


Figure S6: Schematic representation of a prolate ellipsoid with the angles used for the Stoner-Wohlfarth model.  $\theta$  is the angle between the easy axis and the magnetic moment,  $\psi$  is the angle between the external magnetic field and the easy axis and  $\phi$  is the azimuthal angle.  $a$  and  $b$  are the lengths of the semi-major and semi-minor axes. The aspect ratio is  $a/b$ .

Considering a magnetite nanoparticle as a prolate spheroid (Figure S6), the energy of a magnetic state can be calculated using the Stoner-Wohlfarth model as:

$$E = K_{eff}V\sin^2\theta - \mu B(\cos\theta\cos\psi + \sin\theta\sin\psi\cos\phi),$$

where  $V$  is the volume of the particle,  $\theta$  is the angle between the easy axis and the magnetic moment and  $\phi$  is azimuth angle of the magnetic moment  $\mu$  ( $\mu=M_sV$  where,  $M_s$  is the saturation magnetization),  $B$  is the applied external field,  $\psi$  is the angle between the easy axis and the external magnetic field. The effective anisotropy constant  $K_{eff}$  can be written as  $K_{eff} = K_1 + \frac{\mu_0 M_s^2 (N_x - N_z)}{2}$ , where  $\mu_0$  is the vacuum permeability, and  $K_1$  possibly accounts for anisotropy contributions not arising from the shape (such as the magneto-crystalline and surface anisotropy), which we neglect hereafter ( $K_1=0$ ). The second part is the shape anisotropy which we assume to dominate in our case.  $N_x$  and  $N_z$  are the demagnetization factors of the nanoparticle. For spheroidal nanoparticles, the shape anisotropy is determined by the aspect ratio  $k=a/b$ , yielding the following demagnetization factors for the cases of oblate, sphere, and prolate spheroids<sup>3</sup>:

$$N_z = \frac{1}{1-k^2} \left[ 1 - \frac{k}{\sqrt{1-k^2}} \arccos(k) \right], k < 1$$

$$N_z = \frac{1}{3}, \quad k = 1$$

$$N_z = \frac{1}{k^2 - 1} \left[ \frac{k}{\sqrt{k^2 - 1}} \operatorname{arccosh}(k) - 1 \right], \quad k > 1$$

$$N_x = (1 - N_z)/2$$

Hereafter, we model our nanoparticles as prolate spheroids, as the case of oblate spheroids presenting two degenerate axes is marginal. Under thermal equilibrium conditions ( $\tau < t_m$  where  $\tau$  is the residence time in a certain magnetic state and  $t_m$  is the measurement time), the average magnetization with a given orientation ( $\psi$ ) of the easy axis with respect to the external magnetic field direction is given by:<sup>4</sup>

$$m(\psi) = \frac{M}{M_s} = \langle \cos(\theta - \psi) \rangle = \frac{\iint (\cos(\theta - \psi) \cdot \exp\left(-\frac{E}{k_B T}\right) \sin\theta d\theta d\varphi}{\iint \exp\left(-\frac{E}{k_B T}\right) \sin\theta d\theta d\varphi},$$

where  $M_s$  is the saturation magnetization,  $k_B$  is the Boltzmann constant and  $T$  is the absolute temperature. We can get average magnetization curves for different aspect ratios and easy axis orientations using the above equation. Figure 1 of the main text shows different cases of magnetization curves. The case of particle P6 shows a quick saturation of the magnetization for a weak field, with nearly no further increase when the field is further raised. We assign this curve to a particle with its easy axis nearly collinear with the applied field, leading to an early saturation. Particles P2, P3, and to a lesser extent P1, show a steep initial magnetization increase for a weak field, followed by a more gradual increase for higher fields. We assign this behavior to particles with tilted easy axes, which first saturate their magnetic moment along the easy axis, then rotate their magnetization axis upon competition of the anisotropy with the Zeeman energy. In that case, a first saturation along the easy axis gives a component  $M_s \cos\psi$  along the applied field, whereas a further increase of the field moves the magnetization towards the applied field, ending up with projection  $M_s$  on the applied field. Finally, the case of P4 is assigned to a particle whose easy axis is nearly perpendicular to the applied field. No first saturation can be distinguished, and the magnetization gradually rotates from horizontal to vertical along the applied field. For aspect ratios close to 1, the nearly spherical particle magnetizes along the applied field, producing a magnetization curve very similar to that of P6. These behaviors are exactly obtained in the Stoner-Wohlfarth simulations presented in Figure S7, so that angle and aspect ratio can often be determined by visual comparison of the measured magnetization curves to the simulations.

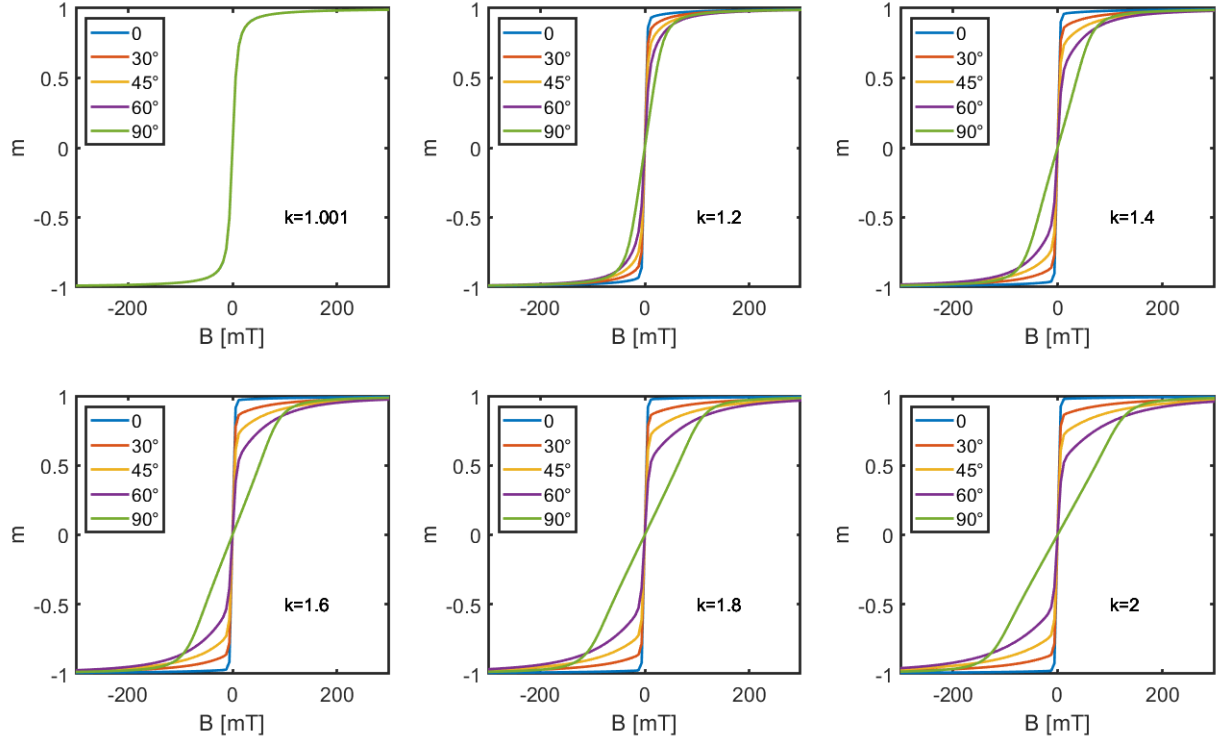


Figure S7: Magnetization curves simulated using the Stoner-Wohlfarth model for particles with different aspect ratios ( $k$ ) and angles ( $\psi$ ) of the easy axis with respect to the external magnetic field.

If the temperature is too low to establish thermal equilibrium on time scales much shorter than the measurement, i.e., if the thermal energy  $k_B T$  allows occasional crossing only of the energy barrier during the measurement, the magnetization will be seen to switch between two states. Then, the population ratio of the two states i.e., the ratio of residence times in the two states follows from Boltzmann statistics as:

$$\frac{\tau_1}{\tau_2} = \exp\left(\frac{E_2 - E_1}{k_B T}\right).$$

Now, using the energy from the Stoner-Wohlfarth model, we can write this ratio for a small enough applied field (i.e., assuming that the applied field is too weak to change the magnetic moment's direction) as:

$$\log\left(\frac{\tau_1}{\tau_2}\right) = \frac{2\mu \cos\psi}{k_B T} B.$$

It turns out that the plots of  $\log\left(\frac{\tau_1}{\tau_2}\right)$  vs.  $B$  are very close to straight lines in all cases, Therefore, if we plot  $\log\left(\frac{\tau_1}{\tau_2}\right)$  vs.  $B$ , we can calculate the magnetic moment ( $\mu_{fit}$ ) as

$$\mu_{fit} = \frac{k_B T}{2 \cos \psi} \frac{d}{dB} \left( \log\left(\frac{\tau_1}{\tau_2}\right) \right)$$

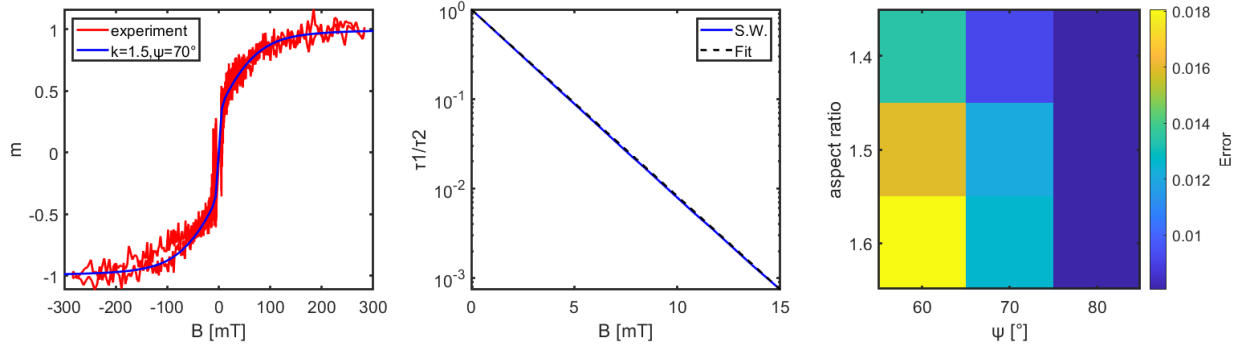


Figure S8: (Left) a magnetization curve fitted with the Stoner-Wohlfarth model. The aspect ratio ( $k$ ) and the angle of the easy axis ( $\psi$ ) are mentioned in the inset. (Middle) The plot  $\log\left(\frac{\tau_1}{\tau_2}\right)$  vs. the external magnetic field ( $B$ ) with a linear fit and with the fit using the Stoner-Wohlfarth model. (Right) The error map for the linear fit and the Stoner-Wohlfarth fit for different values of  $k$  and  $\psi$ .

Figure S9 shows the energy landscape in the XZ plane under an external magnetic field. When there is zero or weak magnetic field, the magnetic moment prefers aligning to the minimum energy direction i.e. along the easy axis. There are two minimum energy points corresponding to up and down spin states as schematically shown in Figure S9. With the increase in magnetic field strength, the energy diagram shifts towards one minimum and the magnetic moment gradually aligns to the magnetic field direction. The rate of the change in the energy diagram with increase in magnetic field depends on the orientation of the magnetic field with respect to the easy axis, i.e., on angle  $\psi$ .



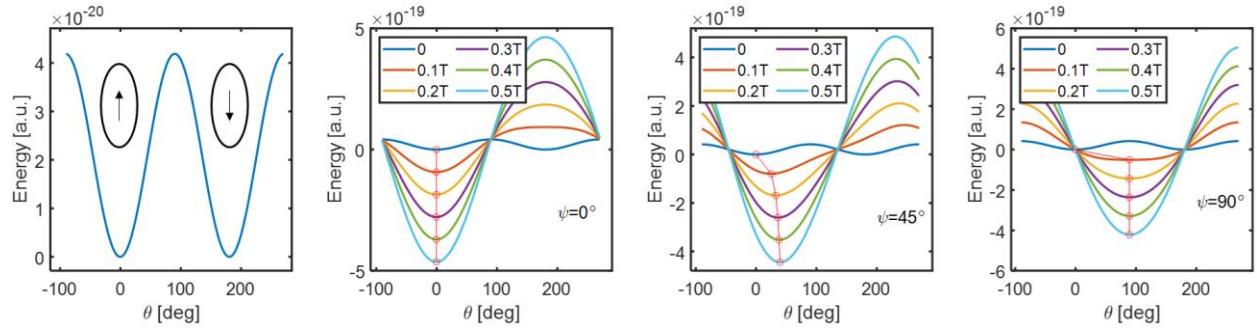
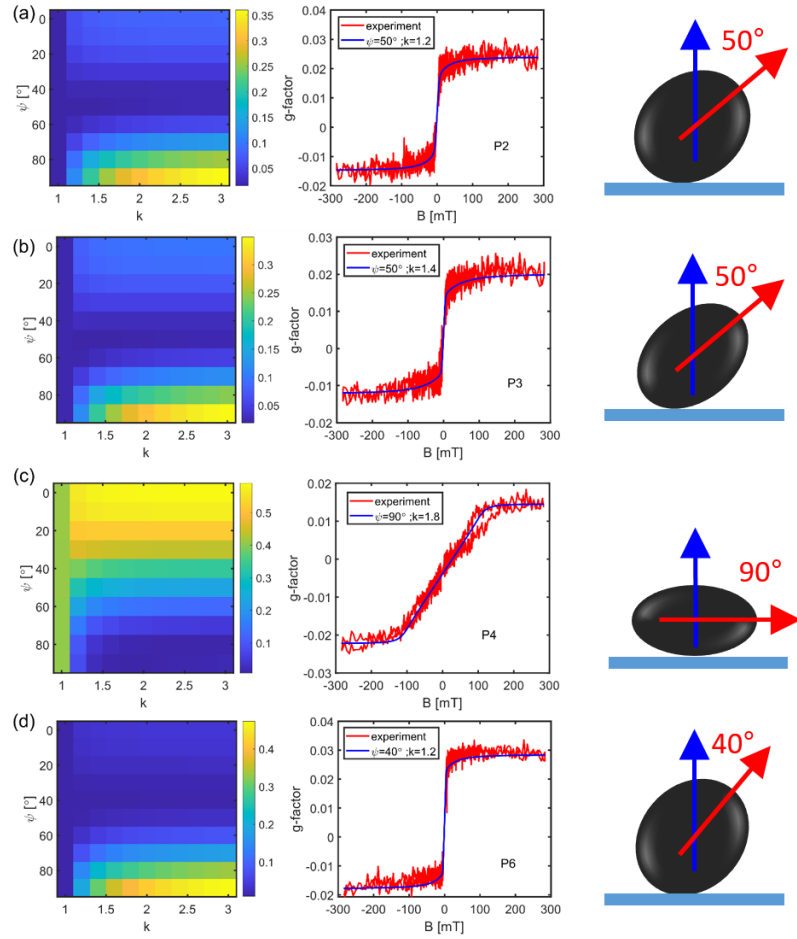


Figure S9: the energy landscape in XZ plane of a single magnetite nanoparticle. (Left) the energy landscape when there is no external magnetic field. (Middle and right) The energy diagram at different field strengths at three different angles of the field orientation w.r.t the easy axis. The red lines with circle show the minimum energy points.

#### Magnetization curves of particles P2, P3, P4 and P6 with Stoner-Wohlfarth fits

Figure S10 shows magnetization curves of particles P2, P3, P4 and P6 as labelled in Figure 1 in the main text. The magnetization curves are fitted with the Stoner-Wohlfarth model considering different aspect ratios ( $k$ ) and angles between the applied magnetic field and the easy axis ( $\psi$ ). The optimized value is obtained by minimizing the error of the fit to the experimental data and shown in the inset of Figure S10 (center).



*Figure S10: Magnetization curves of four particles (P2, P3, P4 and P6 as labelled in Figure 1 in the main text) with Stoner-Wohlfarth fits. (Left) An error map of the fit from the experimental data at different aspect ratios ( $k$ ) and angles between the easy axis and the applied field direction ( $\psi$ ). (Center) The obtained  $k$  and  $\psi$  values obtained for the minimum error are shown in the insets and the corresponding Stoner-Wohlfarth fit (blue) is plotted along with the experimental data (red) is shown. Particle labels are mentioned. (Right) Schematic representation of the magnetic moment (red) along the prolate particle axis for low enough applied magnetic field (blue).*

### Magnetization curves of 32 single magnetite particles

We measured the magnetization curves of 32 single magnetite nanoparticles as shown in Figure S11 and Figure S12. We categorized them in three types, Type I, Type II and Type III. Type I particles are superparamagnetic, Type II particles are with intermediate behaviors i.e., with magnetization switching and Type III particles are ferro(i)magnetic.

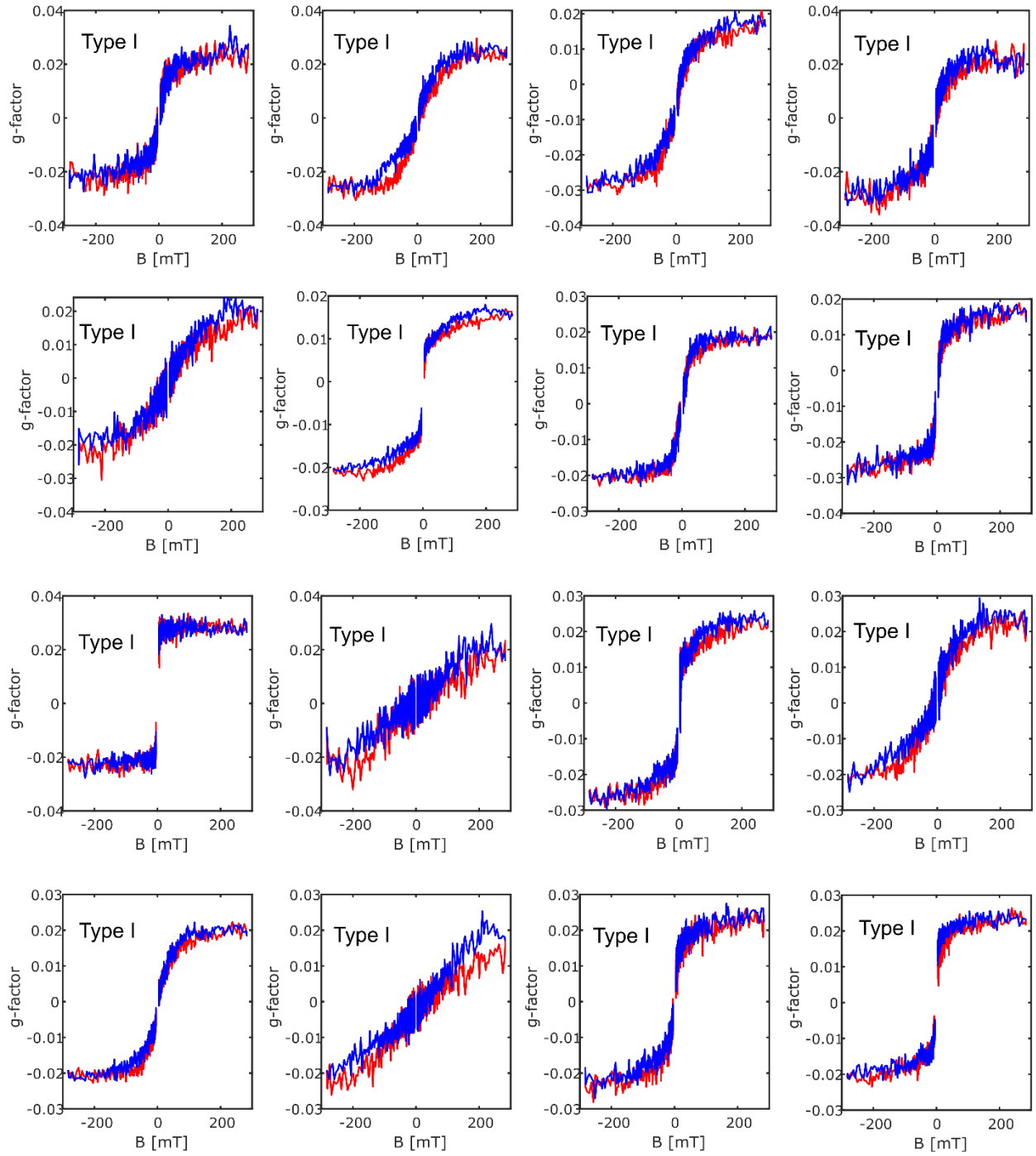


*Figure S11: Magnetization curves of 16 single magnetite nanoparticles of Type I. Red: positive to negative applied magnetic field, blue: negative to positive applied magnetic field.*

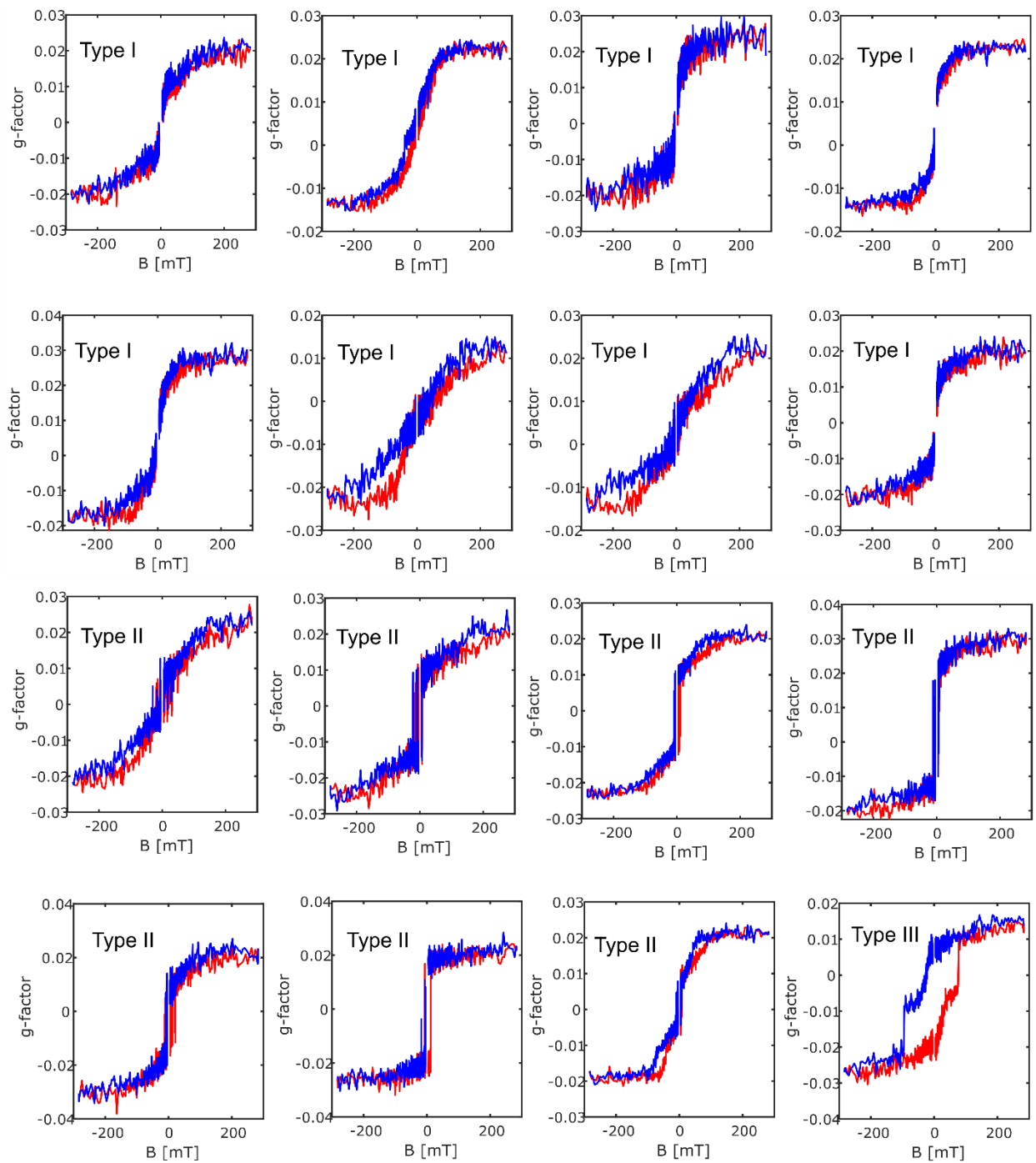


*Figure S12: Magnetization curves of 16 single magnetite nanoparticles of three different types, Type I, Type II and Type III. Red: positive to negative applied magnetic field, blue: negative to positive applied magnetic field.*

### Time traces of PT, CD, LD and LD45 signals for particle P1

Figure S13 shows time traces of photothermal absorption (PT), circular dichroism (CD), and linear dichroism at two different orientations, at  $0^\circ/90^\circ$  (LD) and at  $45^\circ/-45^\circ$  (LD45). Although there are some signal fluctuations for the case of PT, LD and LD45, none of them show signal fluctuations between two states. The only trace showing switching between two states is the CD time trace.

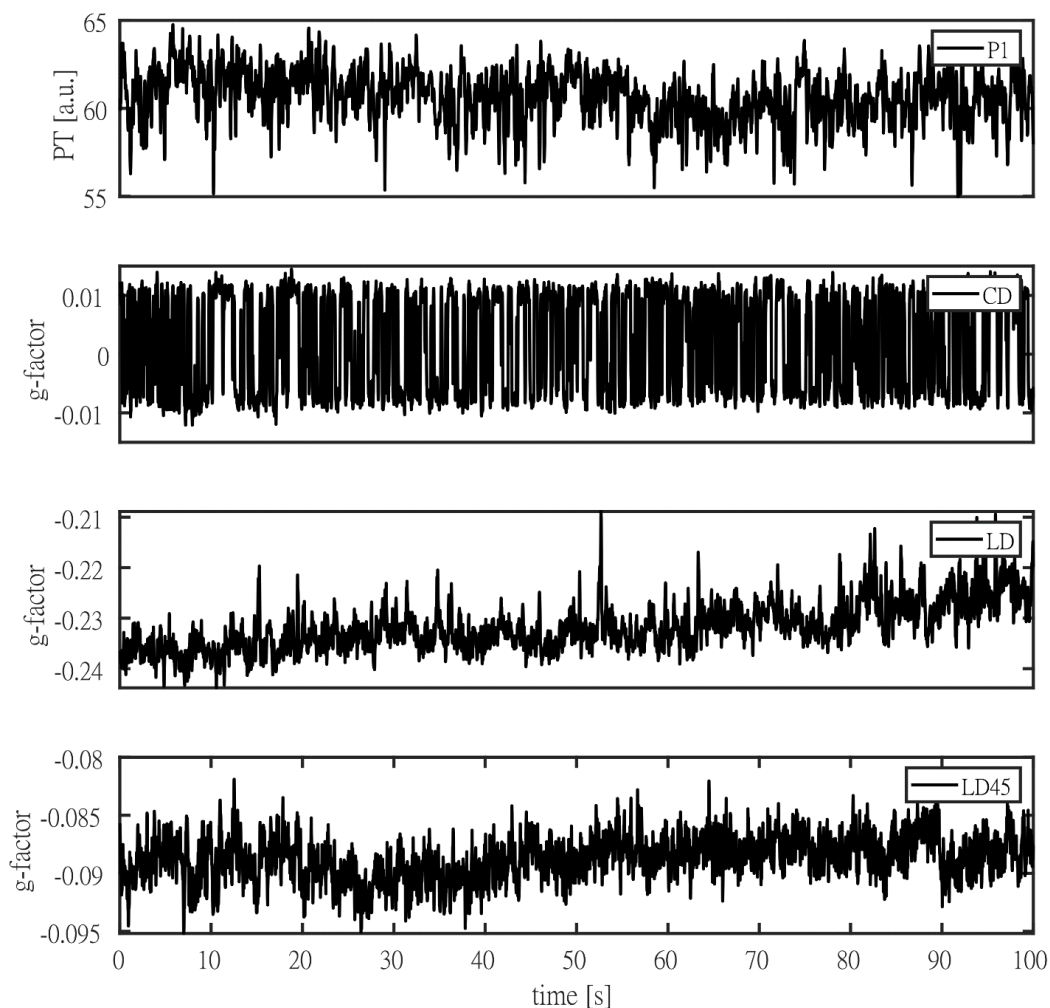


*Figure S13: Time traces of PT, CD, LD and LD45 of particle P1 over 100 s. The slight decrease in LD signal at the end of the time trace is due to slight defocusing. We see signal fluctuation between positive and negative values only for the CD time trace.*

### Threshold analysis of field-dependent switching events for particle P1

Magnetization time traces of particle P1 at different magnetic fields presented in Fig.2 are reproduced here with a threshold analysis (Figure S14). The threshold has been defined to distinguish the two different states and to calculate the residence times in the two states.

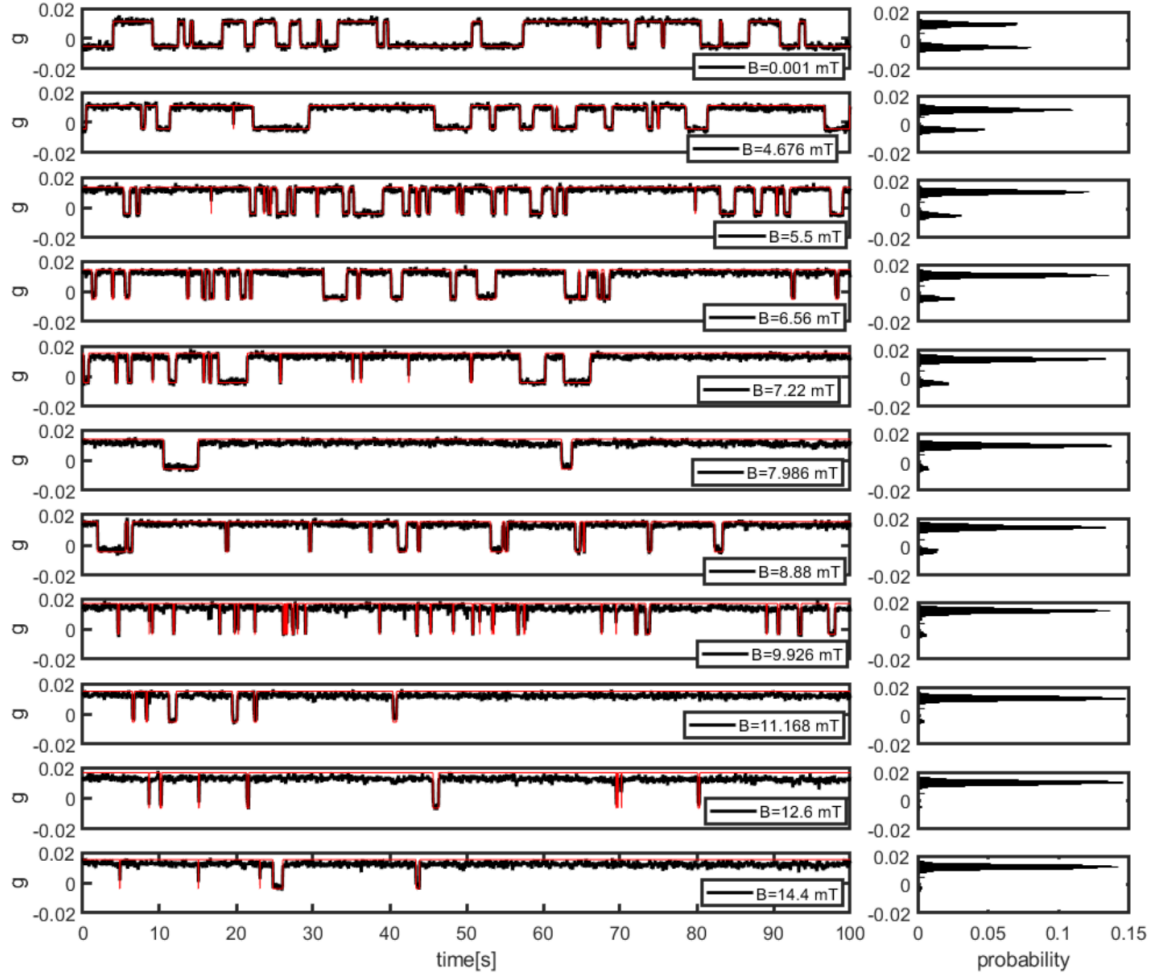


*Figure S14: External magnetic-field-dependent time traces of Fig. 2 of the main text. The threshold is defined to distinguish two states. The fits based on this threshold analysis are shown with solid red lines. The histogram of each time trace is shown on the right.*

### Field-dependent time traces of particles P7 and P8

In the main text, we have shown field-dependent time traces of particle P1 only. Here, we show similar time traces for two more particles, P7 and P8 in Figure S15.



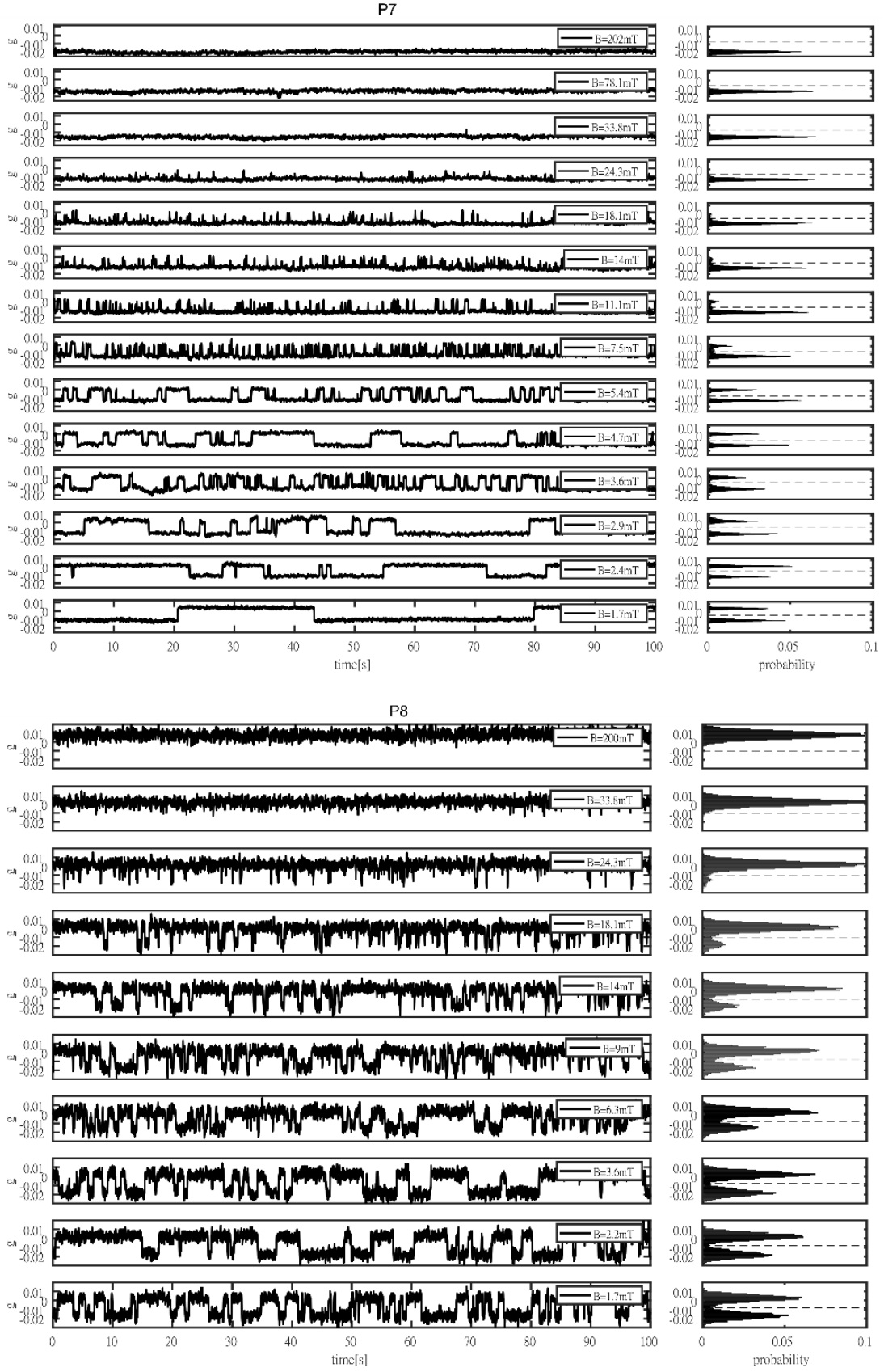


Figure S15: Magnetic-field-dependent time traces of particles P7 and P8.

The ratios of residence times in the two opposite magnetization states of particles P7 and P8 are presented in Figure S16 as a function of the applied magnetic field. For all values of the angle  $\psi$ , the Stoner-Wohlfahrt model gives a very close-to-linear variation with a slope of  $2\mu \cos \psi / k_B T$ . Unfortunately, we did not measure the magnetization curves of these two particles and therefore we do not know the value of  $\psi$ . As can be seen from the time traces of these two particles, fields required to nearly populate only one state, a value which is close to the one found for particle P1 in the main text. Therefore, we assumed  $\psi$  to be close to  $70^\circ$  for particles P7 and P8. Considering  $\psi=70^\circ$ , the magnetic moments for the P7 and P8 are about  $3 \times 10^5$  Bohr magnetons and  $0.95 \times 10^5$  Bohr magnetons. The magnetic moments of P7 and P1 are quite similar, in good agreement with their estimated sizes (23.4 nm diameter for P7 and 24.7 nm for P1). The magnetic moment of particle P8 is about 3 times lower than that of particle P7 which is close to the expected volume ratio, about 4.7. The slight mismatch could be explained by the thickness of their dead layers. As the surface-to-volume ratio is higher for smaller particles, the similar dead-layer thickness would lead to a reduced magnetic moment for smaller particles. The mismatch could also be due to different  $\psi$  values as we do not know the exact  $\psi$  values for these two particles.

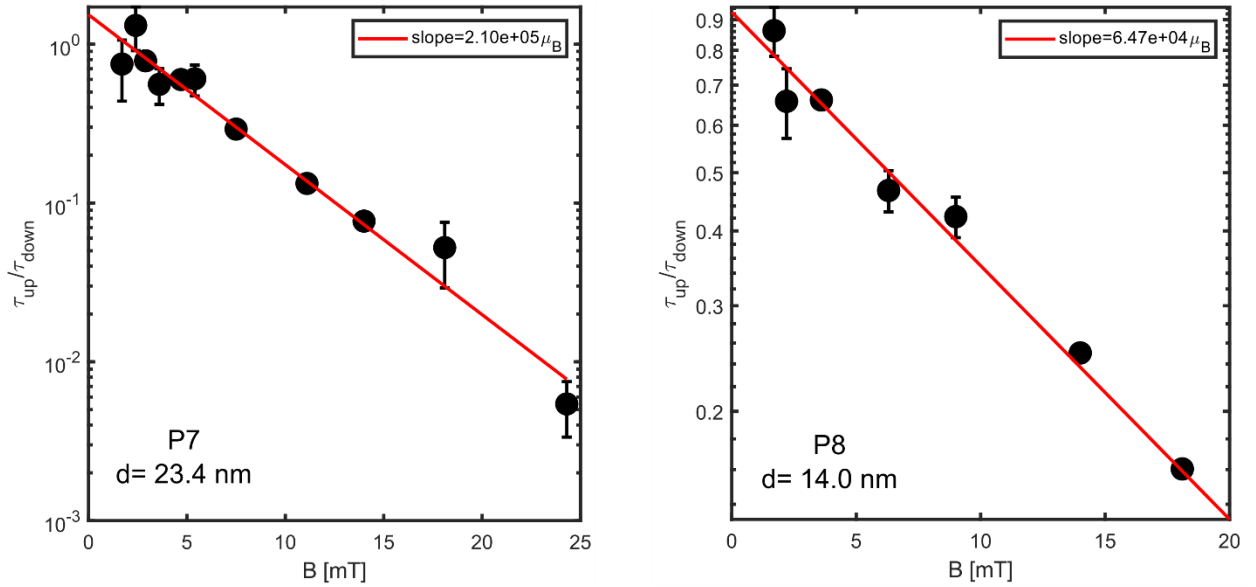


Figure S16: External-field-dependent Boltzmann behavior fitted with the Stoner-Wohlfarth model for particles P7 and P8. The slopes extracted from the fits are  $2.1 \times 10^5$  and  $6.5 \times 10^4$ , respectively. The sizes of the particles are also mentioned in the insets. The error bars are the deviations from the fits.

## Temperature estimation

Simulations of scattering and heat transfer were carried out to calculate the absorbed power and the temperature variation of the nanoparticle, respectively. The nanoparticle scattering model is shown in Figure S17(a). Considering the symmetry of this model, we only take a quarter of the whole model to reduce the calculation time. The particle is at the center of the simulated volume and surrounded by the refractive medium. The mismatch of refractive index between substrate and medium has been ignored. Plane circularly polarized heating and probe beams are taken as background fields. The focusing configurations are different for these two beams, the focus beam waist of the heating beam is 1500 nm and that of the probe beam is 328 nm ( $0.61 \lambda/\text{NA}$ ). The heating and probe powers absorbed by the particle can be obtained by a far-field scattering calculation. To get the temperature of the nanoparticle, we calculate heat diffusion from the nanoparticle to the substrate and medium. The model and boundary conditions are shown in Figure S17(b). The spherical particle is located on the surface of the glass and surrounded by the liquid. Different heat conductivities have been assigned to the glass and to the liquid medium. The particle is set as a point heat source with the power obtained from the scattering simulation. The outside of this model is maintained at ambient temperature (293.15 K). The optical and thermal parameters of materials are shown in Table 1.

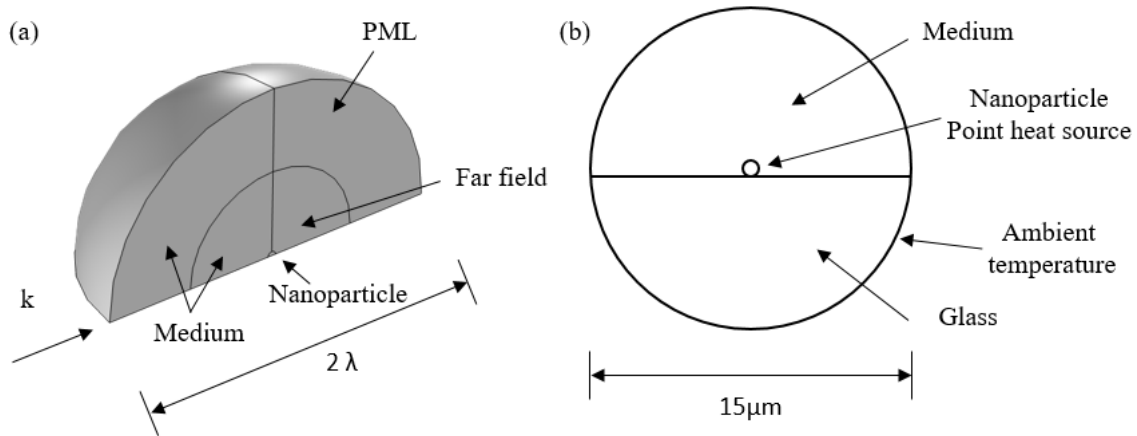


Figure S17: COMSOL model used for the temperature calculation. See details in the text.

	$k$ (W/(m·K))	$C_p$ (J/(kg·K))	$\rho$ (kg/m <sup>3</sup> )	$n$
magnetite	6	890	5180	Huffman/Triaud <sup>5</sup>
glass	1.114	860	2510	1.516
Oil	0.14	1972.5	870	1.518

hexadecane	0.14	2215.1	770	1.433
------------	------	--------	-----	-------

Table 1: Parameters used for the COMSOL simulation to calculate the temperature for magnetite nanoparticles in two photothermal media, oil and hexadecane.

### Probe laser power dependence of the switching events of particle P1

As we vary the particle temperature through variable heating and probe powers, we need the absorption coefficients of magnetite at these two wavelengths to estimate the particle temperature. A number of literature data can be found for the refractive indices of magnetite. Here we selected two values from the works of Huffman et al.<sup>6</sup> and that of Triaud et al.<sup>5</sup> Using the COMSOL model described above, we calculated the temperatures and deduced the residence times in up- and down-states shown in Figure S18. Arrhenius fits to both of these temperature dependences show a similar anisotropy energy barrier. In the main text, we chose the refractive index database of Triaud et al.

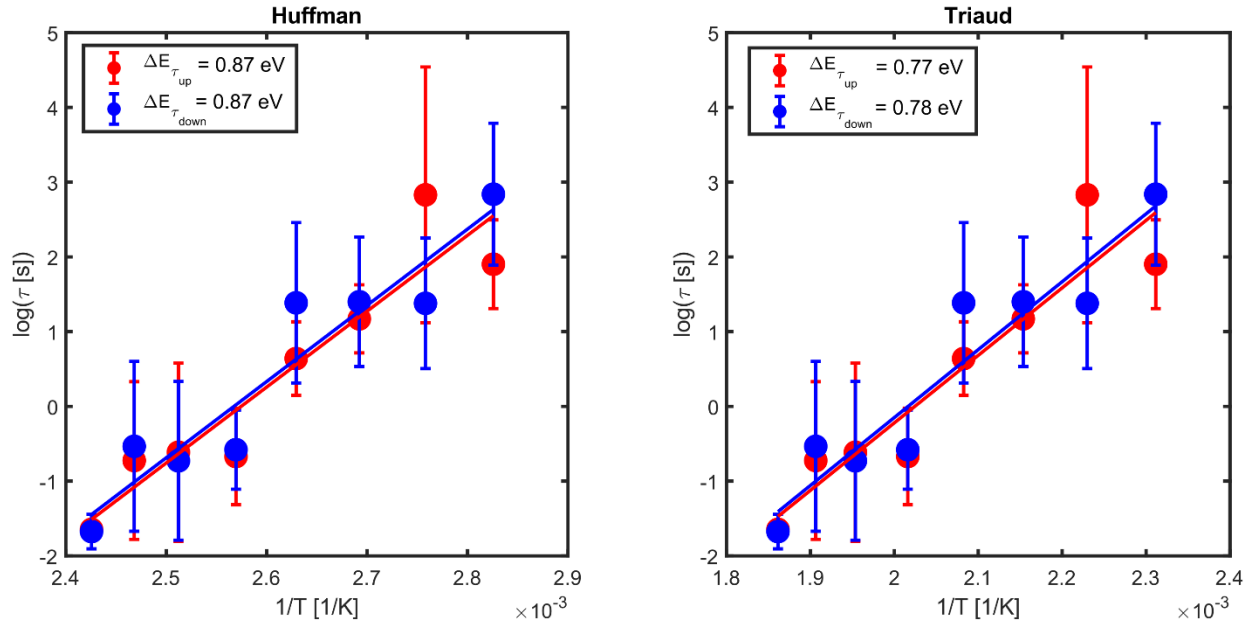
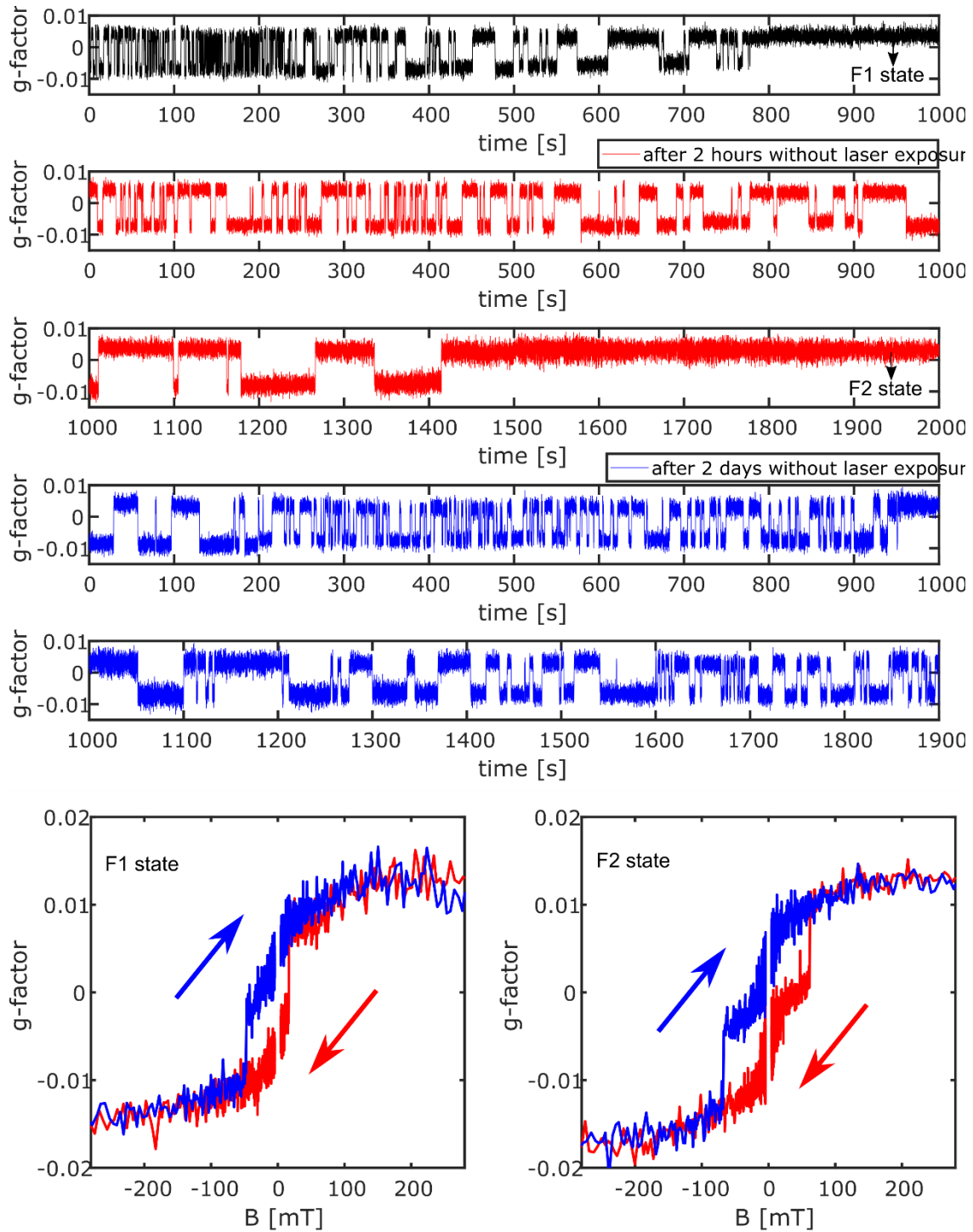


Figure S18: Probe power dependence of residence times in the two magnetization states of particle P1 fitted with the Stoner-Wohlfarth model. The temperature is calculated on the basis of two literature values of the optical absorption of magnetite, by Huffman<sup>6</sup> and Triaud.<sup>5</sup> Both of these temperature dependences yield similar values for the anisotropy energy barrier.

### Dynamical heterogeneity of a particle measured over several hours

To improve the characterization of the dynamical heterogeneity of magnetic switching, we followed a single magnetite nanoparticle (particle A1) for several hours, but not continuously.

We allowed for several waiting times without laser exposure. The results are shown in Figure S19. The particle shows various magnetic behaviors over this longer time period. The mechanism behind the transitions between these behaviors is not well understood. We speculate that composition fluctuations due to possibly reversible (photo-)oxidation events and or structural or surface defects may influence the topography of the magnetic energy landscape, as demonstrated in the simulations by Winklhofer et al.<sup>7</sup>



*Figure S19: Dynamical heterogeneity in the switching behavior of a single particle (A1) measured over several hours. The black time trace shows dynamical heterogeneity over a continuous measurement of 1000 s. The intermediate switching behavior slowly becomes ferromagnetic (F1 state) after 800 s, as evidenced by the hysteresis of the magnetization curve measured in the F1 state (bottom left). After 2 hours without laser exposure, the particle again resumes switching, as shown by the red time trace. Over the next period of 2000 s, the particle reverts to the ferromagnetic (F2) state, as evidenced by the hysteresis loop in the magnetization*



curve measurement of the F2 state (bottom right). After 2 days without laser exposure, the particle resumes switching again and remains in the intermediate switching state for over 1900 s. Arrows indicate the direction of magnetic field sweep.

### Dynamical heterogeneity of UV-plasma-cleaned particles

To check if the surface ligands alone are responsible for the dynamical heterogeneity, we cleaned the magnetite nanoparticles in UV-plasma. Switching measurements of such particles (particle B1 and particle B2) are shown in Figure S20. These particles still show strong dynamical heterogeneity. Therefore, we conclude that surface ligands cannot be the main cause of dynamical heterogeneity.

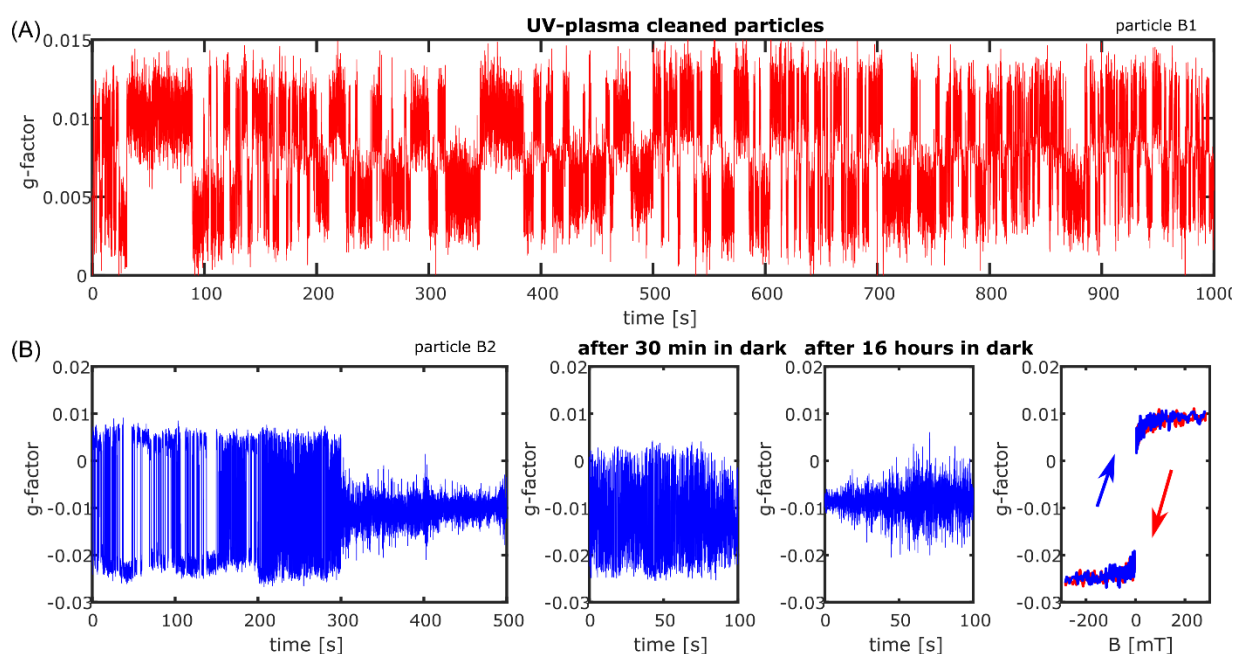


**Figure S20: Dynamical heterogeneity in the switching behavior of two particles (particle B1 and particle B2) which were UV-plasma cleaned.** (A): Particle B1 shows a change of switching rates over time but still remains in the intermediate magnetic state. (B): Particle B2 shows a change from the intermediate switching magnetic behavior to a quickly switching, superparamagnetic state. Without laser exposure for 30 min, the particle seems to slow somewhat in its switching rate, but still remains very fast compared to the earlier intermediate state observed at the beginning of the trace. Here, 16 hours without laser exposure did not change much the superparamagnetic behavior, as evidenced by the hysteresis-free magnetization curve. Arrows indicate the direction of magnetic field sweep.

### Dynamical heterogeneity of a particle covered with HfO<sub>2</sub>

To check whether surface oxidation influences the dynamical heterogeneity behavior of our magnetite nanoparticles, we deposited a thin (5 nm thick) layer of HfO<sub>2</sub> by ALD (atomic layer deposition) which would protect the sample from oxidation. We measured two particles (particle C1 and particle C2) as shown in Figure S21. Both these particles show changes of switching rates over time, and in both cases, the switching rate becomes faster over time. In case of particle C2, we observed three states at the beginning of the trace, which later changed to two states, upon disappearance of one of the states, another possible manifestation of dynamical heterogeneity. The appearance of three states in particle C2 is not understood, and is possibly due to crystalline anisotropy and shape anisotropy both influencing the anisotropy energy barrier for particle C2.

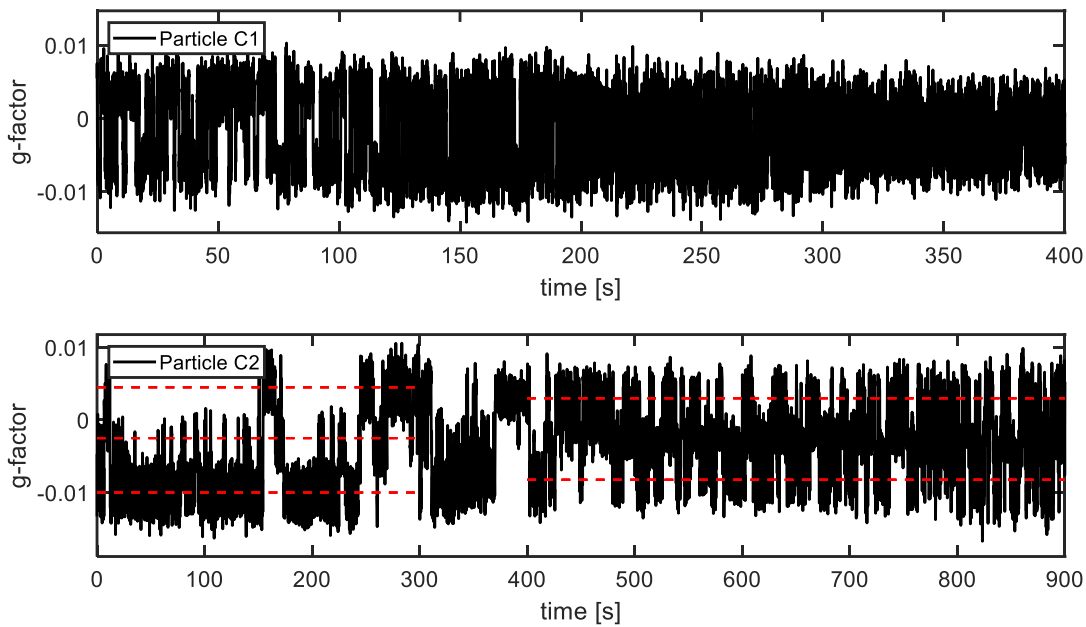


*Figure S21: Dynamical heterogeneity of the switching of two particles (particle C1 and particle C2) measured in a magnetite nanoparticle sample coated by about 5 nm of HfO<sub>2</sub>. Both these particles show changes of switching rates over time i.e., dynamical heterogeneity.*

### Dynamical heterogeneity of a particle which was plasma-cleaned and covered with HfO<sub>2</sub>

To avoid the effects of both surface oxidation and ligands-influence on the dynamical heterogeneity, we prepared a sample which was plasma-cleaned and also covered with 5 nm HfO<sub>2</sub>. We measured time traces of three particles (particle D1, particle D2 and particle D3) as shown in Figure S22. Although particle D2 shows weak dynamical heterogeneity, the other two particles show quite strong dynamical heterogeneity. This result suggests that the changes which induce dynamical heterogeneity are probably taking place inside the particle. Internal charge reordering events upon heating have previously been reported.<sup>8</sup>

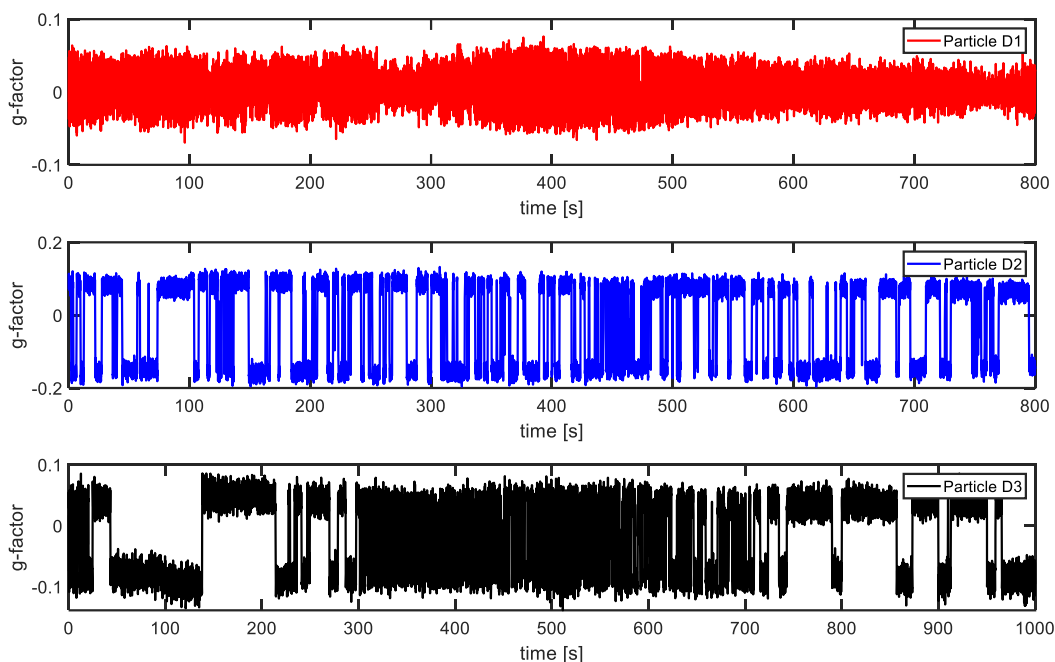


*Figure S22: Time traces of three particles (particle D1, particle D2 and particle D3) measured in a plasma-cleaned sample covered with 5 nm HfO<sub>2</sub>. Time traces showing the dynamical heterogeneity behavior.*

### References:

- (1) Spaeth, P.; Adhikari, S.; Lahabi, K.; Baaske, M. D.; Wang, Y.; Orrit, M. Imaging the Magnetization of Single Magnetite Nanoparticle Clusters via Photothermal Circular Dichroism. *Nano Lett.* **2022**. <https://doi.org/10.1021/acs.nanolett.2c00178>.
- (2) Spaeth, P.; Adhikari, S.; Baaske, M. D.; Pud, S.; Ton, J.; Orrit, M. Photothermal Circular Dichroism of Single Nanoparticles Rejecting Linear Dichroism by Dual Modulation. *ACS Nano* **2021**, *15* (10), 16277–16285. <https://doi.org/10.1021/acsnano.1c05374>.

- (3) Moreno, R.; Poyser, S.; Meilak, D.; Meo, A.; Jenkins, S.; Lazarov, V. K.; Vallejo-Fernandez, G.; Majetich, S.; Evans, R. F. L. The Role of Faceting and Elongation on the Magnetic Anisotropy of Magnetite Fe<sub>3</sub>O<sub>4</sub> Nanocrystals. *Sci Rep* **2020**, *10* (1), 2722. <https://doi.org/10.1038/s41598-020-58976-7>.
- (4) Respaud, M. Magnetization Process of Noninteracting Ferromagnetic Cobalt Nanoparticles in the Superparamagnetic Regime: Deviation from Langevin Law. *Journal of Applied Physics* **1999**, *86* (1), 556–561. <https://doi.org/10.1063/1.370765>.
- (5) Roush, T. L.; Teodoro, L. F. A.; Blewett, D. T.; Cahill, J. T. S. Optical Constants and Diffuse Reflectance of Opaque Minerals: A Modeling Study Using Magnetite. *Icarus* **2021**, *361*, 114331. <https://doi.org/10.1016/j.icarus.2021.114331>.
- (6) Huffman, D. R. Interstellar Grains The Interaction of Light with a Small-Particle System. *Advances in Physics* **1977**, *26* (2), 129–230. <https://doi.org/10.1080/00018737700101373>.
- (7) Winklhofer, M.; Fabian, K.; Heider, F. Magnetic Blocking Temperatures of Magnetite Calculated with a Three-Dimensional Micromagnetic Model. *Journal of Geophysical Research: Solid Earth* **1997**, *102* (B10), 22695–22709. <https://doi.org/10.1029/97JB01730>.
- (8) Elnaggar, H.; Graas, S.; Lafuerza, S.; Detlefs, B.; Tabiś, W.; Gala, M. A.; Ismail, A.; van der Eerden, A.; Sikora, M.; Honig, J. M.; Glatzel, P.; de Groot, F. Temperature-Driven Self-Doping in Magnetite. *Phys. Rev. Lett.* **2021**, *127* (18), 186402. <https://doi.org/10.1103/PhysRevLett.127.186402>.